W7-AS Contributions to the 18th European Conference on Controlled Fusion and Plasma Heating

(Berlin, June 3 - 7, 1991)

IPP III / 179

June 1991

MAX-PLANCK-INSTITUT FÜR PLASMAPHYSIK

8046 GARCHING BEI MÜNCHEN

MAX-PLANCK-INSTITUT FÜR PLASMAPHYSIK

GARCHING BEI MÜNCHEN

W7-AS Contributions to the 18th European Conference on Controlled Fusion and Plasma Heating

(Berlin, June 3 - 7, 1991)

IPP III / 179

June 1991

Die nachstehende Arbeit wurde im Rahmen des Vertrages zwischen dem Max-Planck-Institut für Plasmaphysik und der Europäischen Atomgemeinschaft über die Zusammenarbeit auf dem Gebiete der Plasmaphysik durchgeführt.

W7-AS Contributions to the 18th European Conference on Controlled Fusion and Plasma Heating
(Berlin, June 3 - 7, 1991)

CONTENTS

OPTIMUM CONFINEMENT IN THE WENDELSTEIN 7-AS STELLARATOR

A. Weller, R. Brakel, R. Burhenn, V. Erckmann, P. Grigull, H.-J. Hartfuß
H. Maaßberg, H. Renner, H. Ringler, F. Sardei, U. Schneider
W7-AS Team[1], NBI Team[2], ICRH Group[3], PSI Group[4]

Max-Planck-Institut für Plasmaphysik
Association EURATOM-IPP, D-8046 Garching, Germany

ECRH Group[5]

Institut für Plasmaforschung der Universität Stuttgart
D-7000 Stuttgart, Germany

ABSTRACT

Optimum confinement is realized in WENDELSTEIN 7-AS (low shear modular stellarator, $R = 2\ m$, $a \simeq 0.18\ m$) by wall conditioning and by properly adjusting the parameters determining the magnetic field configuration. In particular low order rational values of the rotational transform have to be excluded from the confinement region or sufficient shear must be established by internal currents. The effective heating of net current free plasmas by ECRF ($P \lesssim 0.8\ MW$, $70\ GHz$) and neutral beam injection (NBI, $P \lesssim 1.5\ MW$, $45\,kV$) involves different plasma parameters and transport regimes. Stationary plasmas are generally produced by ECRF, whereas density and impurity control is a severe problem during NBI. This has initiated different kinds of impurity and particle control scenarios (carbonization, boronization and edge cooling). Thus, $< \beta > \lesssim 1.1\%$ ($1.25\ T$) could be achieved. An extended parameter range with electron temperatures of $200\,eV \leq T_e \leq 3\,keV$, ion temperatures of $100\,eV \leq T_i \leq 0.7\,keV$ and electron densities of $10^{19} \leq n_e \leq 3 \cdot 10^{20}\ m^{-3}$ was accessible. The characteristics of the energy confinement (confinement times up to 35 ms are observed in low power / low density ECRF heated and up to 25 ms in high power / high density NBI heated plasmas) and the particle and impurity transport are described and related to the specific heat and particle sources. The investigations comprise the analysis of electron and ion heat conductivity, particle transport modelling based on H_α measurements at relevant locations around the torus and impurity transport studies by laser blow-off experiments. The influence of the ambipolar electric field is discussed.

KEYWORDS

Stellarator; W7-AS; confinement; impurity control; heat conduction; particle transport; impurity transport; stability.

---

[1]V. Afanasiev[a], J. Baldzuhn, B. Bomba, R. Brakel, R. Burhenn, R. Büchse, G. Cattanei, A. Dodhy, D. Dorst, A. Elsner, M. Endler, K. Engelhardt, V. Erckmann, T. Estrada[b], U. Gasparino, S. Geißler, L. Giannone, G. Grieger, P. Grigull, H. Hacker, H.J. Hartfuß, C. Hidalgo[b], D. Hildebrandt[c], J. Hofmann, A. Izvozchikov[a], R. Jaenicke, J. Junker, F. Karger, M. Kick, K. Kondo[d], H. Kroiss, G. Kühner, I. Lakicevic, A. Lazaros, H. Maaßberg, C. Mahn, K. Mc Cormick, H. Niedermeyer, W. Ohlendorf, H. Renner, H. Ringler, N. Ruhs, J. Saffert, J. Sanchez[b], F. Sardei, S. Sattler, F. Schneider, U. Schneider, G. Siller, U. Stroth, M. Tutter, F. Wagner, A. Weller, H. Wolff[e], E. Würsching, M. Zippe, S. Zöpfel.
[2]W. Ott, F.P. Penningsfeld, E. Speth.
[3]M. Ballico, F. Hofmeister, J.M. Noterdaeme, F. Wesner.
[4]R. Behrisch, A. Martinelli, V. Prozesky, J. Roth, E. Taglauer.
[5]W. Kasparek, G.A. Müller, P.G. Schüller, M. Thumm[e]

[a]Ioffe Institute, Leningrad, USSR [b]CIEMAT, Madrid, Spain [c]Zentralinstitut für Elektronenphysik, Berlin, Germany
[d]Plasma Physics Laboratory, Kyoto University, Japan [e]Kernforschungszentrum Karlsruhe, Germany

INTRODUCTION

The W7-AS "Advanced Stellarator" (major radius $2\,m$, plasma radius $\leq 0.18\,m$) is in operation since summer 1988 (Renner, 1989, Ringler, 1990). The configuration of W7-AS with $m = 5$ periods, similar to 5 toroidally linked mirrors, is produced by a system of modular coils. This concept results in an optimization with respect to equilibrium and transport. A superimposed variable toroidal and vertical field provide flexibility to modify the magnetic parameters: range of rotational transform $0.25 \leq \iota \leq 0.7$, shear and magnetic well. Different edge conditions, limiter or separatrix dominated, can be established, depending on the choice of ι and the limiter position.

The equipment for heating includes ECRH (4 gyrotrons at $70\,GHz$ with 200 kW each), NBI (tangential injection with 1.5 MW), ICRH (preliminary antenna system with $1\,MW$). Recently experiments using a gyrotron at $140\,GHz$ (developed by the KfK Karlsruhe) with pulse duration of $100\,ms$ and a power of $100\,kW$ were initiated. A plasma of $\bar{n}_e = 1.3 \cdot 10^{19}\ m^{-3}$ and $T_e(0) = 860\ eV$ could be sustained. The higher cut-off density for $140\,GHz$ enables combined heating with ECRF and NBI up to densities of $1.2 \cdot 10^{20}\,m^{-3}$. First tests were carried out using ICRF as a start-up scenario. Target plasmas with $\bar{n}_e = 2 \cdot 10^{19}\ m^{-3}$ for NBI-heating could be produced from neutral gas filling at a magnetic field down to $0.6\,T$ independent on the magnetic resonance conditions. Therefore, experiments with NBI became possible in a wide range of the magnetic field without restrictions imposed by ECRF at the corresponding resonance field of $1.25\,T$ or $2.5\,T$, respectively.

The progress on W7-AS is based on the improved control of the magnetic configuration and, in particular, on the measures to reduce the impurities. A detailed discussion on results of wall conditioning, plasma wall interaction and impurity radiation analysis will be given in the first section of this paper. Plasma heating and confinement under improved wall conditions are described in the next section, which includes a discussion of effects of the magnetic configuration with emphasis on high-β operation. This part stresses the extended parameter range and compares the global confinement time with different scaling laws. The following section deals with local transport studies. For low and moderate densities ($n_e \lesssim 8 \cdot 10^{19}\ m^{-3}$) χ_e and χ_i have been deduced separately and compared with neoclassical expectations. At higher densities, where $T_i \simeq T_e$, the total energy balance is analyzed. The influence of the ambipolar electric field is taken into account.

In the next section a comparison of ion fluxes from the DEGAS-code with neoclassical predictions is made in the particle transport analysis. Flux averaged neutral density profiles are obtained from DEGAS simulations and discussed for NBI discharges. The last chapter gives a detailed discussion of impurity transport studies using laser ablation. The local transport parameters characterized by diffusion coefficient and convection velocity are derived from transport simulations. The experimental data are also related to neoclassical impurity transport predictions. Finally the results are summarized and conclusions are drawn.

IMPURITY AND PARTICLE CONTROL

Wall Conditioning Procedures

W7-AS was initially operated with unconditioned metallic walls (except of baking and periodic He glow discharge conditioning (GDC)). Impurity radiation predominantly arose from oxygen, carbon, titanium and iron. ECR-heated plasmas were critically affected by radiation losses at low input power or densities near the cut-off limit. The parameter range accessible with NBI-heating was severely limited to medium densities ($n_e(0) \lesssim 8.0 \cdot 10^{19}\ m^{-3}$) and correspondingly low temperatures ($T_e(0) \lesssim 600eV$) by a radiation collapse from metallic impurities (Fig. 1).

The impurity situation could be considerably improved by coating the vacuum vessel with carbon or boron layers, respectively. The layers were deposited during glow discharges on the vessel walls at room temperature ($5h$ deposition time). Carbonization was done in gas mixtures of about 70% He + 30% CH_4 or CD_4, respectively. The deposited carbon layer reached a thickness of $\simeq 1000\mathring{A}$. The four boronization runs were performed in mixtures of 90% He + 10% B_2H_6 (Winter, 1990). Prior to the first boronization the carbon layer was removed from the surfaces by a hydrogen glow

discharge. The boron layer reached a thickness of 500–800Å. Surface analysis of a removable probe yielded a mixture of about 60% boron, 30% hydrogen and 10% carbon.

Plasma Wall Interaction

W7-AS is equipped with two vertically movable main limiters (TiC-coated graphite, each $0.25m^2$) placed in neighbouring field periods at the top and bottom apexes of the elliptic cross-section. At low ι the configuration is limiter-dominated, whereas when increasing ι above 1/2 it is separatrix-dominated for retracted limiter positions.

For $\iota \geq 1/2$ the boundary topology is determined by $5/m$ resonances due to the fivefold magnetic field periodicity and the pentagonal shape of the magnetic axis (formation of "natural" islands). This gives rise to enhanced localized particle and energy outflow to the wall and in-vessel installations from the X-points (positions depending on ι) and, independent of ι, along a helical contour at the radial outside (Rau, 1990, Grigull, 1990). Due to short connection lengths these fluxes cannot be efficiently screened by the main limiters.

The main limiter thermal load for comparable discharges is strongly increased after wall boronization or a fresh carbonization (by up to a factor 2.5 in both cases) and reaches 60% of the absorbed input power (ECRF or NBI, low ι, low density). It is decreased with increasing ι, density and limiter aperture.

The main limiters are the dominating impurity source (Ti, C, O, from spectroscopic data) for limiter-determined operation. With decreasing limiter action, walls and, especially, certain erosion dominated areas where the flux bundles mentioned above intersect some installations (partially screened by graphite) become increasingly competitive and are dominating in the separatrix regime (Fe, C, O). This wall contact enhances the boundary radiation as well as the radiative losses from the core and establishes a severe limitation of the accessible parameter range.

Impurity Radiation Analysis

Impurity fluxes will be qualitatively discussed on the basis of VUV-spectra of intermediate ionization stages (CIII, OV, TiXII, FeXVI) obtained by the SPRED spectrometer and by the analysis of long-term integrating deposition probes (Brakel, 1991).
Immediately after a new carbonization (Philipps, 1989) of the metallic vessel a significant reduction was observed for all impurity species. A persistent suppression of Ti- and Fe-radiation could be obtained for discharges with high density and low temperature (NBI, Fig. 1b compared to 1a). Erosion of the carbon layer on the limiters causing a re-increase of Ti, however, occurred during higher power and low density discharges. O- and C-fluxes generally rose after initial reduction (as compared to metallic walls) to their former levels typically within 30 shots, indicating O-enrichment in the fresh carbon layer followed by O- and C-release via CO-desorption and chemical sputtering. Simultaneously the recycling fluxes steadily increased and density control became impossible. The properties of a fresh carbon layer could efficiently be restored by He-GDC.

Boronization (Winter, 1989, Schneider, 1990) reduced both, O and C, durably because of the O-gettering effect of boron and the associated breaking of the CO-desorption cycle. For all operational regimes a permanent reduction of C and O radiation (CIII, OV) by factors of 50-100 was observed directly after a fresh boronization and by a factor of 5-10 after more than 100 shots under steady state wall conditions (Fig. 2). As a consequence of reduced low-Z radiation losses the plasma edge temperature rose significantly with boronized walls from typically $\lesssim 50\ eV$ to $\gtrsim 100\ eV$ (in addition to reduced impurity fluxes, the reduction of the edge radiation, as shown in Fig. 2, is also caused by increased edge temperatures). The limiter thermal loads are thereby considerably enhanced and the boron coating is supposed to be eroded from the limiters within a few shots. Limiter erosion is evident from Fig. 2 by the fast increase of TiXII and CIII emission directly after boronization. The Ti radiation even rises by a factor of $\simeq 2$ above its pre-boronization value. The transient maximum in the evolution of Fe-emission is assumed to be caused by the release of Fe, which has been deposited on the limiters during the conditioning glow discharge. Redistribution of wall material by GDC has already been observed earlier (Grigull et. al, 1990). The persisting reduction of Fe by a factor of $\simeq 2$ demonstrates wall protection by the boron

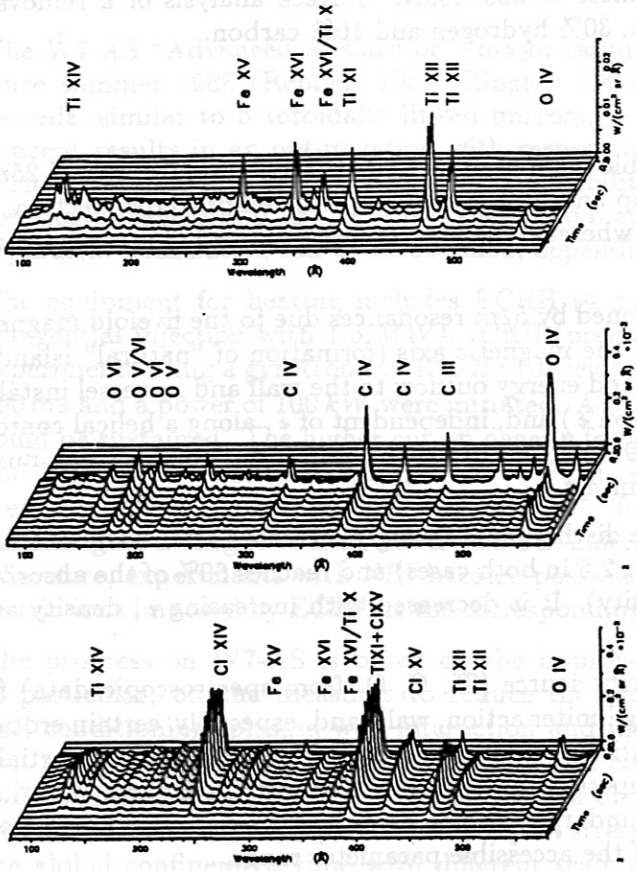

Fig. 1. VUV spectra of plasma impurities for NBI-heated discharges under different wall conditions (from SPRED spectrometer). Top (a): stainless steel wall, middle (b): after first carbonization, bottom (c): after second boronization. The scale is enlarged by 5 for case (a). $P_{NBI} = 1.7MW, B = 2.5T, \iota = 0.34, z_L = 0.315m$.

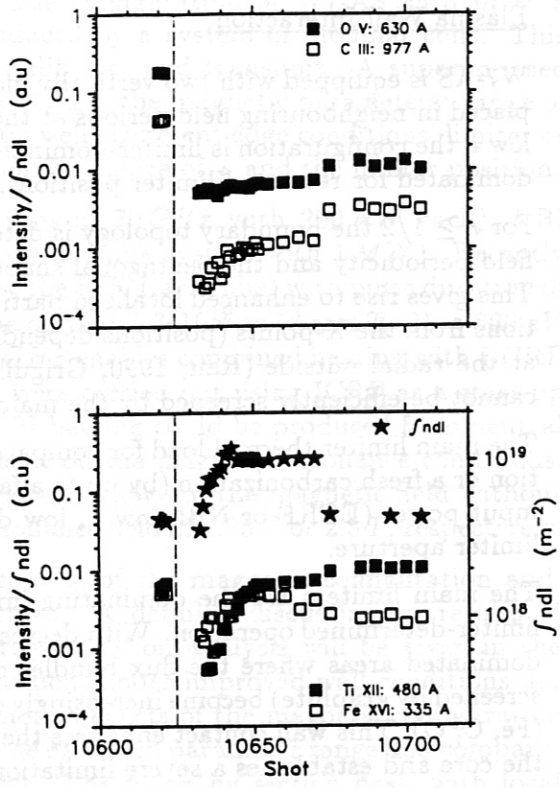

Fig. 2. Impurity radiation normalized to $\int n_e dl$ as observed by SPRED and $\int n_e dl$ in response to the first boronization after #10624. $P_{ECRF} = 180\,kW, \iota = 0.34$.

coating. Soft-X spectra from the plasma center show the same trends (Brakel et al, 1991). After boronization strong gas puffing was required to lower the edge temperature and thus to reduce the Ti-influx. Impurity survey spectra under these conditions are shown in Fig. 1c.

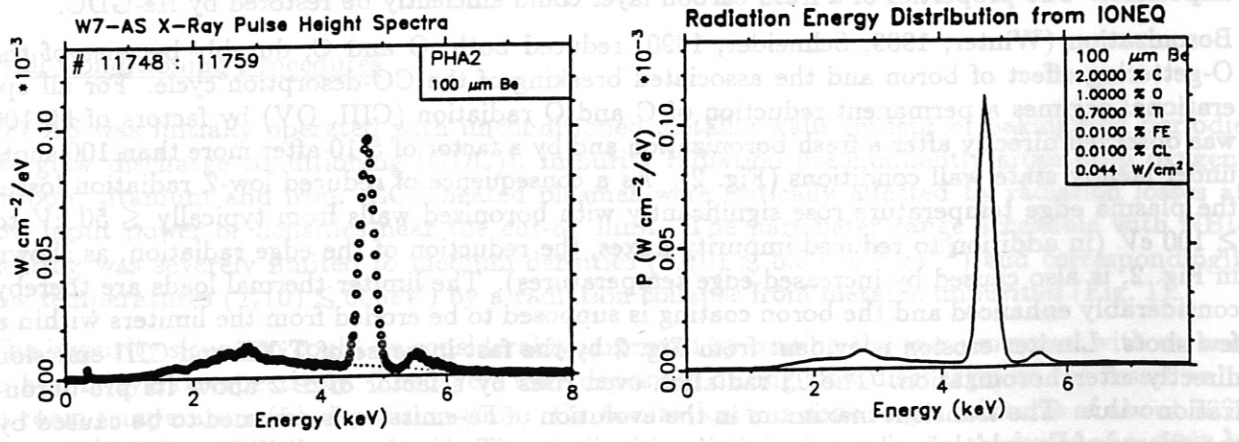

Fig. 3. Experimental (left) and simulated (right) PHA-spectra after boronization showing Ti-lines at 4.7 keV. $P_{ECRF} = 360kW, B = 2.5T, \iota = 0.35$

Impurity concentrations are derived from modelling the intensities measured by various absolutely calibrated radiation monitors (Soft-x cameras, Bragg spectrometer, bolometer system) with the IONEQ code (Weller et al., 1987 and 1990). Impurity transport coefficients derived from Al-injection, T_e-, n_e-, and T_i-profiles and neutral gas profiles from DEGAS code (Heifetz, 1982) calculations (Sardei, 1991) are input to the code. The impurity concentrations (O, C, Fe) are adjusted for the best fit of calculated and experimental data. Ti-concentrations are derived separately from the simulation of He- and H-like lines appearing in PHA-spectra including satellite lines (Fig. 3). Spectroscopic information on central C-emission is not yet routinely available and a ratio of C:O$\simeq$2:1 has been assumed which is consistent with the rise of respective CXRS-lines at the switch-on of the neutral beams.

Table 1. Typical impurity concentrations in % of the central electron density for stainless steel (SS) and boronized (B) vessel ($\sim$ 80 shots after boronization) and the resulting Z_{eff}. ($P_{ECRF} = 350\,kW, n_e = 3 \cdot 10^{19} m^{-3}, \iota = 0.35$).

	Shot	C	O	Ti	Fe	Z_{eff}
SS	10548	6	3	0.3	0.02	5
B	10728	1	0.6	0.6	0.01	4

Impurity concentrations in stationary ECRF-discharges are compared in Table 1 before and after boronization. A significant reduction after boronization is observed for C, O, and Fe whereas Ti increases by a factor of $\simeq 2$. Therefore, no significant change in Z_{eff} occurs. With increasing density and sufficient edge cooling (NBI) the impurity concentrations reduce to values corresponding to $Z_{eff} \simeq 1.3$. The effect of wall conditioning observed in the spectroscopic data agrees well with measurements of particle fluxes by collector probes in the SOL.

PLASMA HEATING AND CONFINEMENT UNDER IMPROVED WALL CONDITIONS

Effects of the Magnetic Configuration

In the low shear stellarator optimum confinement in ECRF-discharges is obtained for values of the rotational transform at the boundary $\iota(a)$ in the close vicinity of 1/3, 1/2, and 2/3. Field perturbations at the plasma edge reduce the particle confinement and increase the recycling. The edge temperature reacts particularly sensitively to the destruction of the magnetic surfaces. Low order rational values of ι within the bulk plasma also deteriorate the confinement as indicated by flattening of the temperature profiles, if not sufficient shear is established (Renner, 1990). Depending on the plasma parameters a net current is observed which is identified as the bootstrap current. Therefore, the profile of the vacuum rotational transform becomes modified by the Pfirsch-Schlüter (PS) currents and pressure driven net-currents of up to $7 - 8\ kA$, as confirmed by neoclassical calculations of the bootstrap current based on measured profiles. Usually the experiments were performed with the condition $I_p = 0$ (net-current-free) with low order rational values of $\iota(a)$ excluded. By compensating the bootstrap current either by ohmic currents or by central current drive (ECCD) positive shear is generated at higher temperatures. In this case "resonances" always exist inside the plasma and perturbations due to mode activity or local fluctuations are detected by magnetic probes, ECE-, soft X-measurements and reflectometry.

Proceeding to higher β and densities, the sensitive dependence of the confinement properties on the boundary value of the rotational transform becomes smoothed out. For typical NBI discharges, the β profiles are rather broad with strong gradients close to the plasma radius, a. In this regime, the PS currents introduce significant shear, the effect of the bootstrap and Ohkawa currents is only small due to the low temperatures. However, the confinement was found to be insensitive to additional OH currents which change the shear at the plasma edge. Changes of the ι profile are indicated by changes of the mode activity, which, however, is not related to the global confinement properties. In the NBI discharges, the collisionalities are higher, $\nu^* > 0.1$. With increasing ν^*, island formation and field ergodization are expected to play only a minor role

for the heat transport. The main loss channel turned out to be the ion heat conduction. For very high ν^*, the pressure profile is even broader than the plasma radius defined by the main limiter aperture (see Fig. 5). However, further detailed investigations have to clarify these phenomena.

In spite of a reduced Shafranov shift as consequence of reduced Pfirsch-Schlüter currents in W7-AS (Renner, 1990), it was necessary to control the plasma position by superimposed vertical fields during operation at high plasma pressure and low rotational transform ($\iota \simeq 1/3$) in order to prevent impurity release by the contact of the plasma with installations inside the vessel.

In the NBI heated plasmas two characteristic kinds of mode activity depending on the ι profile have been found by X-ray cameras and magnetic pickup coils. At moderate densities $m = 3$ modes at $\iota \simeq 1/3$ and $m = 2$ modes at $\iota \simeq 1/2$ could be identified, which appear to be related to a population of fast injected particles, as indicated by an extremely short decay time ($\sim 0.5\ ms$) after the NBI switch off (Lazaros, 1991). In the range of highest β-values ($< \beta > \simeq 1\%$, see next section) low frequency oscillations ($\sim 4\,kHz$) are detected in the X-ray emission. So far no influence of these modes on the global confinement could be seen.

Parameter Range

"Currentless plasmas" are produced by ECRF and heated by ECRF or NBI and combined. An extended parameter range under improved wall conditions with electron temperatures of $200\,eV \leq T_e \leq 3\,keV$, ion temperatures of $100\,eV \leq T_i \leq 0.7\,keV$ and electron densities of $10^{19} \leq n_e \leq 3 \cdot 10^{20}\ m^{-3}$ was accessible (Fig. 4).

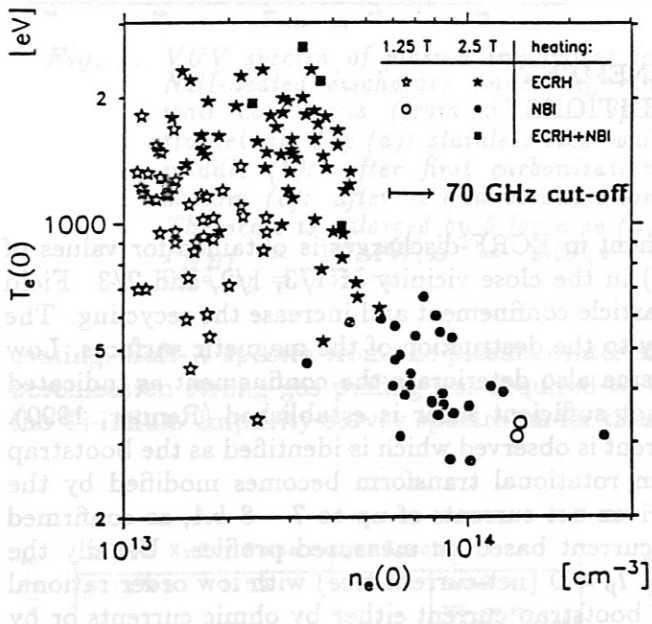

Fig. 4. Parameter Range of n_e and T_e (full profile database).

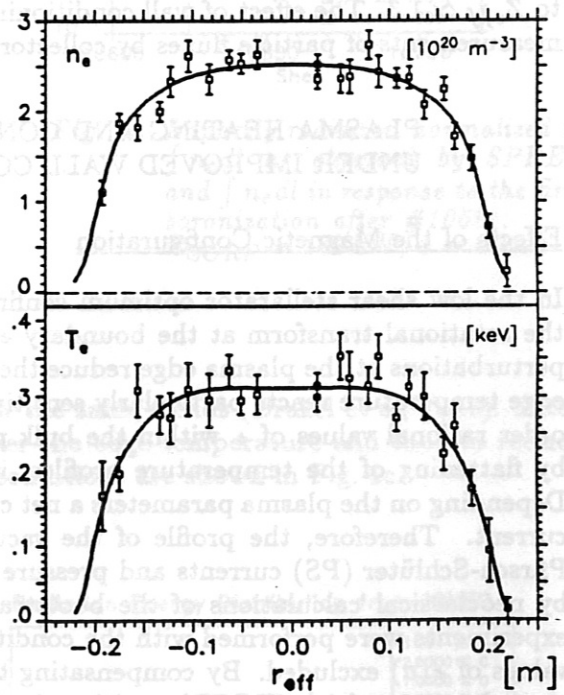

Fig. 5. Measured Profiles of n_e, T_e for NBI heating at $B = 2.5\,T$, $\iota = 0.35$, $P_{NBI} \simeq 1.5\,MW$.

For a main field of $2.5\ T$ and rotational transform $\iota \simeq 1/3$, volume averaged β-values of $< \beta > \simeq 0.7\%$ were achieved. In accordance with observed energy confinement scaling (see next section) β is raised almost entirely by increasing the density, and reaches the highest β-value of $< \beta > \simeq 1.1\%$ at $B = 1.25\ T$ under reduced confinement conditions.

The confinement and transport studies covered various parameter regimes: ECRF-plasmas at low collisionality $10^{-3} \leq \nu^* \leq 10^{-2}$ are found to be dominated by electron heat transport. For NBI plasmas at higher densities ($\nu^* \geq 10^{-1}$) electrons and ions are stronger coupled and the

ion heat conduction becomes dominant. Whereas for ECRF at $70\,GHz$ the density is limited to $6 \cdot 10^{19}\ m^{-3}$ by cut-off, the density of NBI plasmas can be increased to extremely high values up to $3 \cdot 10^{20}\ m^{-3}$, depending on the available power and the radiative losses. For the case of NBI with a power of $1.5\,MW$ measured profiles of a well documented discharge are shown in Fig. 5. In this high density case ($n_e(0) \simeq 2.5 \cdot 10^{20}\ m^{-3}$) the T_e and n_e profiles are significantly broader than those of equivalent discharges with lower n_e. Close to the limiter, the mean free path is much smaller than the connection length ($\nu^* \simeq 5$). Then the limiter plays only a minor role for the particle and energy balance, which is confirmed by H_α and limiter calorimetry observations. In this high density regime the effective plasma radius can exceed the limiter radius.

The density limit is determined by the radiation and increases strongly (almost linearly) with NBI power after boronization / carbonization. At temperatures of $\sim 250\,eV$ usually a thermal collapse is observed. The impurity mix and content can be significantly influenced by controlling the heating power and the external gas flux and by wall conditioning. After boronization the impurity concentrations reduce to values corresponding to $Z_{eff} \simeq 1.3$ at high densities with sufficient edge cooling by neutral flux. In the limiter regime (at $\iota \simeq 1/3$), the highest densities and lowest radiative losses could be reached.

According to the transport models improved confinement was expected at higher rotational transform. However, the beneficial effect of the higher rotational transform was only observed at moderate densities in the initial phase of the discharge. Apparently, operating in the separatrix regime, the uncontrolled power and particle flow to the wall and the internal installations (depending on the magnetic configuration and the plasma parameters) leads to an increased impurity level.

Global Confinement Scaling

Maximum energy confinement times, $\tau_E{}^{exp}$, were found in discharges with high densities at low heating power level. For optimum confinement, $\tau_E{}^{exp}$ scales with a^2 where a is the effective plasma radius, however, confinement degradations due to low order rational values of the rotational transform (causing a reduction of the plasma radius) can play an important role (Ringler, 1990).

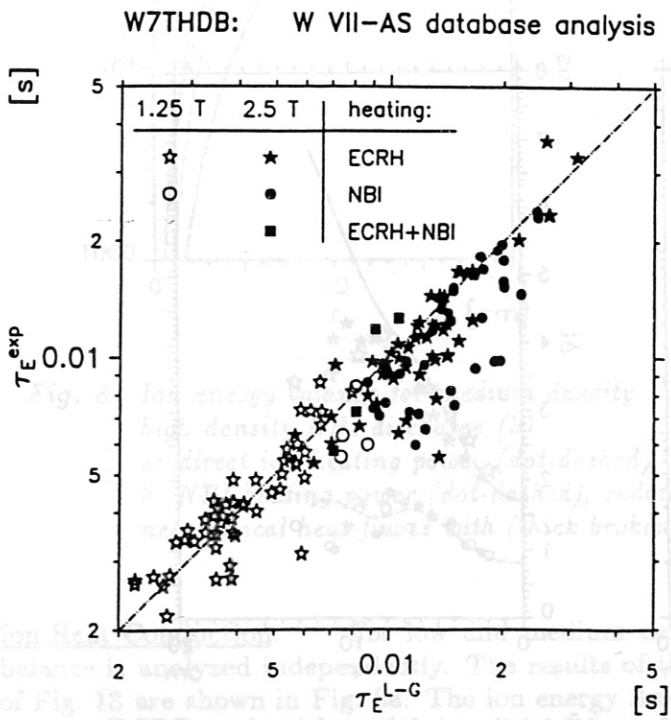

Fig. 6. Energy confinement times from experiment, $\tau_E{}^{exp}$, versus the Lackner-Gottardi scaling, $\tau_E{}^{L-G}$.

In Fig. 6, $\tau_E{}^{exp}$ is compared with the prediction of a tokamak L-mode scaling law (K. Lackner and N.A.O. Gottardi, 1990) which is based on a model of neoclassical ion plateau transport, here,

the plasma current is replaced by the rotational transform:

$$\tau_E^{L-G} = 0.17 \cdot R \cdot a^2 \cdot B^{0.8} \cdot \iota^{0.4} \cdot (\langle n_e \rangle / P)^{0.6}$$

Furthermore, the model of drift wave turbulence used for ATF results as well as the empirical LHD scaling mainly based on HELIOTRON-E experimental results were tested: the average deviation of $\tau_E{}^{exp}$ is typically less than 50 %. The results are similar because the dominating dimensional dependence is in accordance with gyro-reduced Bohm scaling. Use of the Goldston L-mode scaling, on the other hand, leads to complete disagreement: the increase of $\tau_E{}^{exp}$ with density is not reproduced. In Fig. 6, the energy confinement time is independent of the heating method (ECRF, NBI and combined). In these discharges, the line averaged density is between 0.08 and $2.5 \cdot 10^{20}$ m^{-3}, the central electron temperature between 0.25 and 3 keV, the heating power between 0.12 and 1.6 MW. Both the electron and the ion energy transport can be the major loss channels: the electron energy transport dominates in the low and the ion energy transport in the high density regime (see next section). Consequently, the fact that $\tau_E{}^{exp}$ in Fig. 6 is reproduced by only a single scaling law for this wide range of discharge parameters is remarkable.

LOCAL TRANSPORT STUDIES

Electron and Ion Energy Transport

Electron Heat Conduction. The electron energy balance is analyzed for discharges with lower densities ($n_e < 8 \cdot 10^{19}\, m^{-3}$) for which the collisional electron-ion coupling can be estimated from measured T_e and T_i profiles. A purely diffusive ansatz is used for the electron heat conduction: $q_e = -n_e \chi_e{}^{exp} T_e'$. The experimental heat conductivities, $\chi_e{}^{exp}$, were found to be significantly larger than the neoclassical predictions (Ringler et al., 1990). Only for high T_e ($> 1.5\, keV$ in ECRH discharges) at low n_e, $\chi_e{}^{exp}$ in the core region is comparable with the neoclassical one (LMFP regime). For optimum confinement in ECRH discharges (central power deposition) with nearly constant T_e gradients, values of about $0.2\, m^2/s$ are found. $\chi_e{}^{exp}$ decreases with n_e and increases with the global heating power. So far, no conclusive local scaling could be obtained. Furthermore, the electron heat conduction seems to be independent of the heating method (ECRH, NBI and combined).

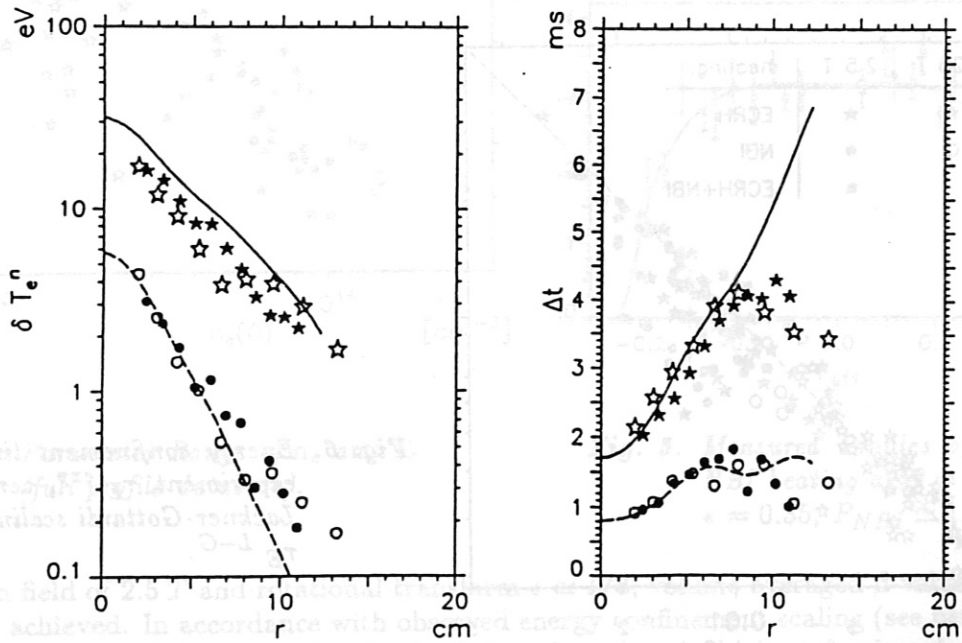

Fig. 7. Measured amplitudes and time delays of $\tilde{T}_e(r)$ (symbols) resulting from ECRH power modulation ($f_{mod} = 69\ Hz$) and simulation (lines): fundamental (stars and solid lines) and 3rd harmonic (circles and broken lines), data from low (open symbols) and high field side (full symbols).

The analysis of electron heat wave propagation generated by ECRH power modulation is also used for estimating χ_e^{exp} (Hartfuß et al., 1986 and 1991). Square wave modulation of the ECRH power (only odd harmonics of f_{mod}) with typically 10% amplitude results in an electron temperature modulation, $\tilde{T}_e(r)$, measured by the ECE diagnostic. The amplitude and the time delay (phase shift) of $\tilde{T}_e(r)$ evaluated by cross correlation technique is analyzed by means of the linearized electron energy balance (non-linear effects leading to even harmonics of f_{mod} were not observed). First evaluations indicate that χ_e^{exp} from the heat wave analysis correspond to the values obtained from the stationary power balance. As shown in Fig. 7 for an ECRH discharge at low heating power ($P_{ECF} = 120\,kW$, $n_e(0) \simeq 5 \cdot 10^{19}\,m^{-3}$ and $T_e(0) \simeq 650\,eV$) the measured amplitudes and time delays of $\tilde{T}_e(r)$ for both the fundamental and the 3rd harmonic were reasonably well reproduced by the simulation taking also into account minor modifications introduced by off-axis power deposition according to ray-tracing calculations. For these simulations, the χ_e^{exp} profile from the stationary power balance was used. $\chi_e^{exp} \propto T_e^{3/2}$ was assumed for the temporal dependence, though, this assumption is not very significant for this example. The deviations at outer radii where the coherence becomes smaller are sensitive to the shape of the χ_e^{exp} profile and the additional power deposition. For the low modulation frequencies ($f_{mod} = 69\ Hz$ in Fig. 7), the assumption of temporal constant T_i and n_e may also be violated.

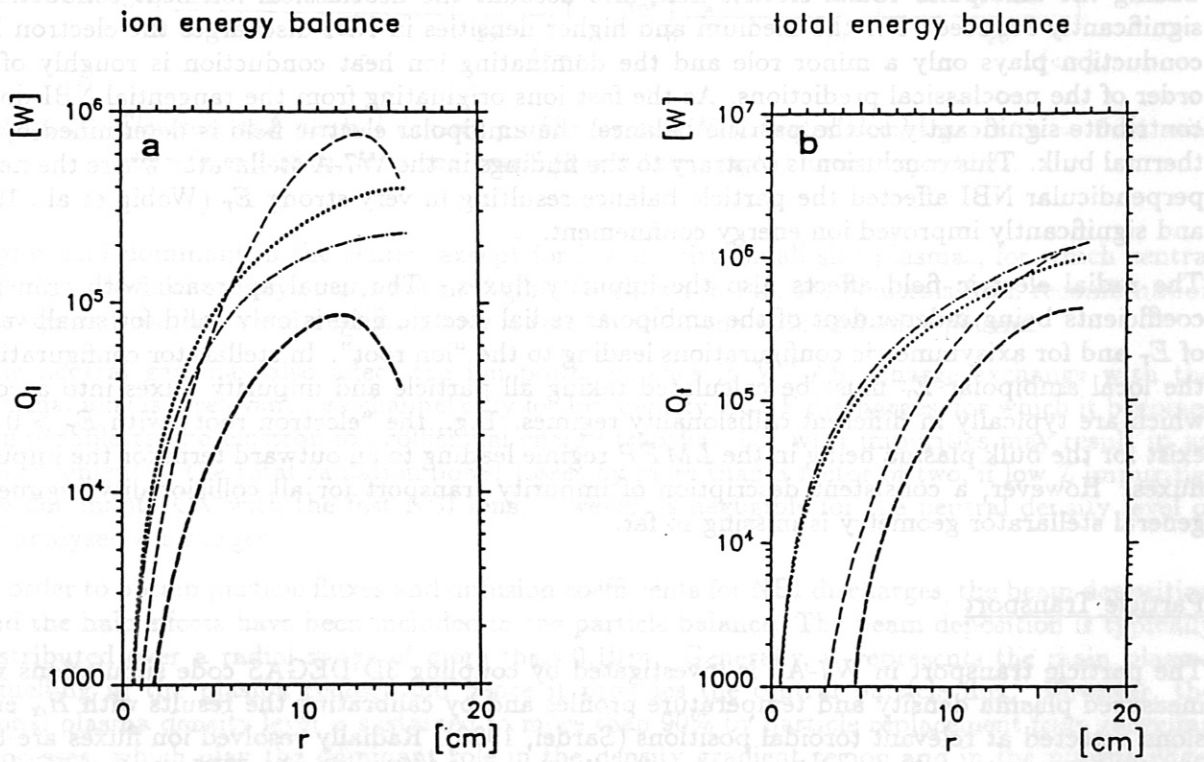

Fig. 8. *Ion energy balance for medium density NBI discharge (a) and total energy balance for high density NBI discharge (b).*
a: direct ion heating power (dot-dashed), including P_{ei} (dotted),
b: NBI heating power (dot-dashed), radiation subtracted (dotted),
neoclassical heat fluxes with (thick broken) and without E_r (thin broken line).

Ion Heat Conduction. For low and medium densities ($n_e < 8 \cdot 10^{19}\ m^{-3}$) the ion energy balance is analyzed independently. The results of the ion energy balance for the NBI discharge of Fig. 18 are shown in Fig. 8a. The ion energy fluxes are estimated by means of direct heating in NBI discharges (dot-dashed line), collisional ion heating, P_{ei}, and CX losses which turned out to be rather small in the bulk part of the plasma. The ion heat conduction is compared with the neoclassical prediction based on DKES code calculations (van Rij and Hirshman, 1989). Typically, the neoclassical fluxes without assuming a radial electric field, E_r, turned out to be too large (thin

broken line in Fig. 8a). Using the ambipolarity condition with impurity fluxes omitted, E_r was calculated. Disregarding the LMFP collisionality regime, negative values of E_r were found ("ion root") leading to a significant reduction of the neoclassical ion heat conduction (thick broken line). The experimental values are typically between these two theoretical predictions (Afanasiev et al., 1991).

For higher densities ($n_e > 10^{20}\,m^{-3}$) where $T_i \simeq T_e$ can be assumed, the total energy balance in which the coupling term P_{ei} disappears is analyzed leading to an effective heat conductivity, χ^{eff} which is compared with the neoclassical prediction of the ion transport. In the very high density discharges (see Fig. 5) with the maximum energy content obtained so far, the profiles are untypically flat in the central region indicating enhanced transport. With the assumption of $T_e \approx T_i$ in the analysis, χ^{eff} is much larger than χ_i^{neo} in the central part as indicated by the very small T_i and n_e gradients. For this case, the total energy balance is shown in Fig. 8b. The integrated NBI heating power, which is obtained from beam deposition calculations (Penningsfeld, 1991), is slightly reduced by radiation and exceeds significantly the total neoclassical fluxes with and without E_r in the central part. The analysis is only reliable within the effective limiter radius of about $0.18\,m$, the profiles are broader. In the regime of stronger gradients ($r > 0.12\,m$) χ^{eff} is close to χ_i^{neo} and the energy losses are mainly determined by the ion transport.

Taking the ambipolar radial electric field into account the neoclassical ion heat conduction is significantly reduced. For the medium and higher densities in NBI discharges the electron heat conduction plays only a minor role and the dominating ion heat conduction is roughly of the order of the neoclassical predictions. As the fast ions originating from the tangential NBI do not contribute significantly to the particle balance, the ambipolar electric field is determined by the thermal bulk. This conclusion is contrary to the findings in the W7-A stellarator where the nearly perpendicular NBI affected the particle balance resulting in very strong E_r (Wobig et al., 1987) and significantly improved ion energy confinement.

The radial electric field affects also the impurity fluxes. The usual approach with transport coefficients being independent of the ambipolar radial electric field is only valid for small values of E_r and for axisymmetric configurations leading to the "ion root". In stellarator configurations, the local ambipolar E_r must be calculated taking all particle and impurity fluxes into account which are typically in different collisionality regimes. E.g., the "electron root" with $E_r > 0$ can exist for the bulk plasma being in the $LMFP$ regime leading to an outward term for the impurity fluxes. However, a consistent description of impurity transport for all collisionality regimes in general stellarator geometry is missing so far.

Particle Transport

The particle transport in W7-AS is investigated by coupling 3D DEGAS code simulations with measured plasma density and temperature profiles and by calibrating the results with H_α emissions detected at relevant toroidal positions (Sardei, 1990). Radially resolved ion fluxes are then obtained from the calculated ion source distributions. Additionally for NBI discharges, radial profiles of the neutral beam halo and of the beam deposition are taken from FAFNER code (Lister, 1983) calculations. Several NBI discharges with 350 to 1500 kW heating power and different plasma densities and limiter apertures have been analyzed and compared with ECRF discharges.

The flux surface averaged neutral density profiles, as obtained from the DEGAS simulations, are shown in Fig. 9 for two NBI discharges at $\iota(a) = 0.34$, where closed vacuum magnetic surfaces exist even at larger radii than determined by the limiters. In the first case (Fig. 9a), where the limiter was retracted near to the wall ($a = 0.18\,m$), the heating power was twice as high and the gas puffing six times as strong as in the other case. This resulted in a high density plateau up to the plasma edge. (The edge temperatures were comparable in both cases.) This implies a significantly higher plasma outflux and, consequently, higher neutral density in the scrape-off layer (SOL). Most of these neutrals are ionized within a narrow radial range about the limiter, due to the screening effect of the high density plasma. Limiter and wall recycling contribute almost equally to plasma refuelling in this case. In the small limiter aperture case ($a = 0.125\,m$, Fig. 9b), the limiter recycling is dominant. The beam halo is generally negligible in the outer plasma

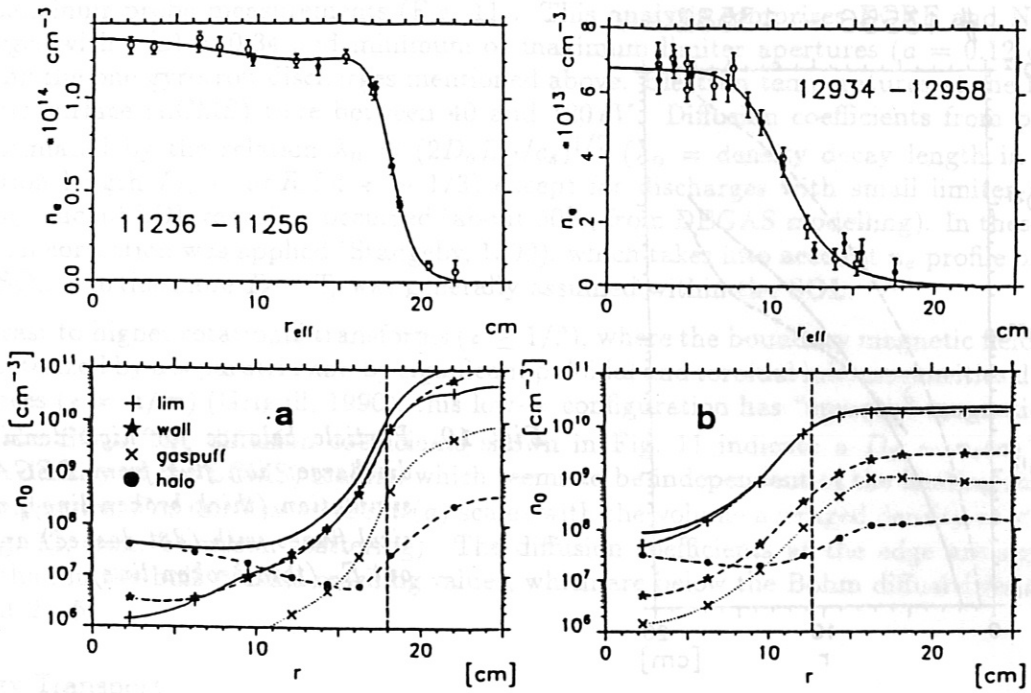

Fig. 9. Electron and neutral density profile for two NBI heated discharges at $\epsilon = 0.34$ with large ($a = 0.18\,m$, left) and small ($a = 0.12\,m$, right) limiter apertures.

region and dominant in the center, except for low density, small size plasmas, for which central refuelling by limiter recycling is not negligible, as shown in Fig. 9b. Neutrals from recombination are ignored, as they yield negligible source rates both in the bulk and edge plasma.

The neutral gas may also affect the ion power balance in W7-AS. Charge exchange with the thermal ions is a relevant loss channel only for low density ECRF discharges, for which it becomes comparable to the electron-ion collisional energy transfer. CX with impurities may result in an enhancement of the total radiation power losses by more than a factor of two, if low Z impurities are dominant. CX with the fast NBI ions, however, is negligible for the neutral density level of all analyzed discharges.

In order to obtain particle fluxes and diffusion coefficients for NBI discharges, the beam deposition and the halo effects have been included in the particle balance. The beam deposition is typically distributed over a radial range of more than $0.10\,m$. Generally, it represents the main plasma refuelling in the plasma center, and hence it provides the central particle flux. However, the global plasma density level is sustained to more than 90% by particle replacement from recycling processes, which play the dominant role in the density gradient region and in the plasma edge. (Refuelling rates of $1.5 \cdot 10^{20}\,s^{-1}$ from $700\,kW$ NBI input power compare, for example, to limiter and wall recycling rates between 30 and 100 times larger, depending on plasma density and limiter position.)

A comparison of the ion fluxes, as simulated by DEGAS code, with neoclassical predictions with and without ambipolar electric field (ion root, $E_r < 0$) (Afanasiev,1991) is shown in Fig. 10 for the high density NBI discharge already discussed in the previous section (see Figs. 5,8). The neoclassical ion fluxes without electric field are about one order of magnitude larger than the ambipolar fluxes. A comparison of the ion fluxes, as simulated by DEGAS code, with the ambipolar neoclassical predictions shows a reasonable agreement throughout the bulk of the plasma up to the limiter. The gap between the two fluxes towards the plasma edge, which is usually found for lower densities (Sardei, 1990), disappears in this case. This is due to the very broad high density profile (see Fig. 5) , which leads to high Pfirsch-Schlüter fluxes at the plasma edge. An uncertainty of up to a factor of two cannot be excluded in the calibration of the simulated fluxes in this case of maximum limiter aperture, as the recycling processes at the wall and secondary

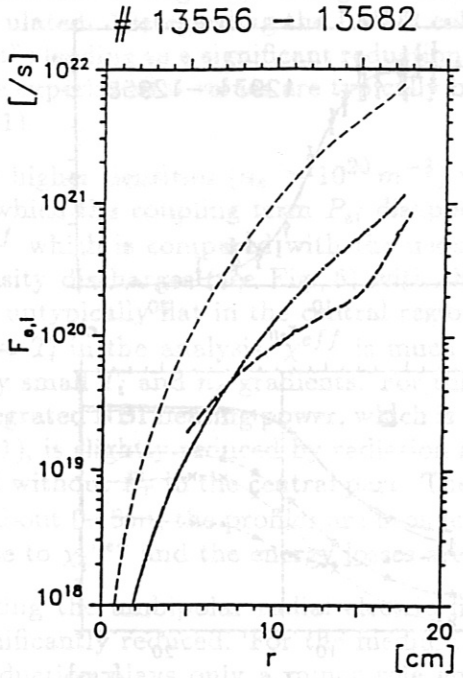

Fig. 10. Particle balance for high density NBI discharge: ion flux from DEGAS code simulation (thick broken line), neoclassical fluxes with (dot dashed) and without E_r (thin broken line).

limiters strongly depend on inhomogeneities close to the wall.

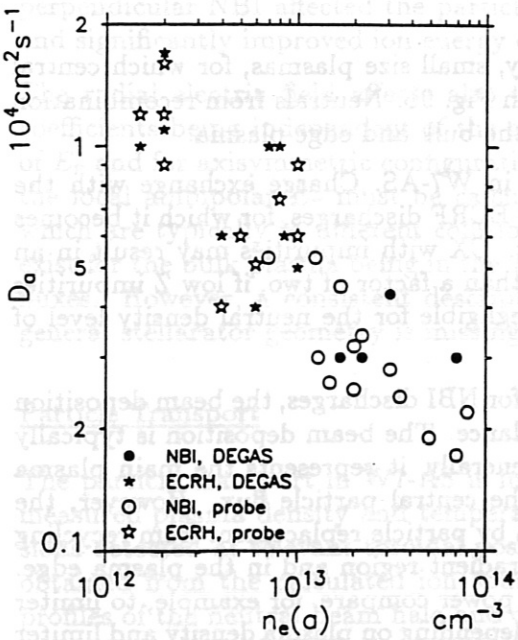

Fig. 11. Particle diffusion coefficients at the last closed magnetic surface from DEGAS code modelling and Langmuir probe data $\iota = 0.34$ vs. LCMS plasma density n_{ea}.

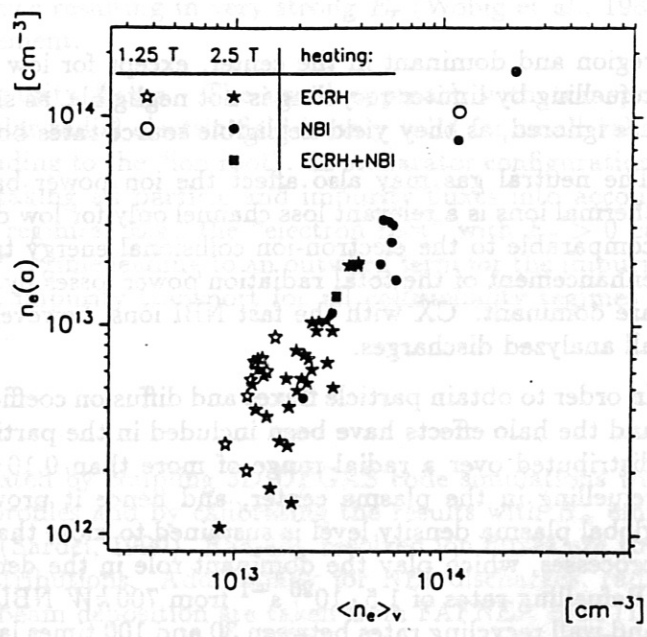

Fig. 12. Edge density n_{ea} vs. volume averaged density for ECRF and NBI plasmas with $\iota \simeq 1/3$ and limiters in outward position.

The diffusion coefficient is obtained from the ion fluxes by using the simple diffusive ansatz $\Gamma = -Dn'$. Estimated Z_{eff} were used to derive the ion density profiles. A comparison of equivalent ECRH discharges (1 gyrotron, $\iota(a) \simeq 0.34$ and 0.52) before and after boronization indicates that the diffusion coefficient has the same dependence on the local density, and is quite insensitive to changes of the impurity concentrations and of the electron temperature (T_e higher after boronization). This is consistent with the density scaling of D at the edge, as derived

from Langmuir probe measurements (Fig. 11). This analysis comprises ECRF and NBI heated discharges with $\iota(a) \approx 0.34$ and minimum or maximum limiter apertures ($a = 0.12$ or $0.18\,m$) including the one gyrotron discharges mentioned above. Electron temperatures at the last closed magnetic surface (LCMS) were between 40 and $120\,eV$. Diffusion coefficients from probe data were estimated by the relation $\lambda_n = (2D_a L_C/c_s)^{1/2}$ (λ_n = density decay length in the SOL, connection length $L_C \approx 3\pi R$ for $\iota \sim 1/3$) except for discharges with small limiter apertures, where significant SOL recycling occurred (about 50%, from DEGAS modelling). In these cases an analytical correction was applied (Stangeby, 1990), which takes into account n_e profile broadening in the SOL. Furthermore $T_e = T_i$ was generally assumed within the SOL.

In contrast to higher rotational transforms ($\iota \geq 1/2$), where the boundary magnetic field topology is characterized by a separatrix and by significant poloidal and toroidal inhomogeneities due to $5/m$ resonances ($\iota = n/m$) (Grigull, 1990), this low-ι configuration has "smooth" magnetic surfaces within the SOL. The diffusion coefficients shown in Fig. 11 indicate a $D_a \sim n_e(a)^{-1/2}$ (n_{ea} electron density at the LCMS) scaling, which seems to be independent of the heating scheme and limiter aperture. For this low ι case $n_e(a)$ scales with the volume averaged density as $< n_e >_v^{1.28}$ (see Fig. 12, from Thomson scattering). The diffusion coefficients at the edge are significantly higher than in the bulk plasma reaching values, which are below the Bohm diffusivities by factors of about 2 - 5.

Impurity Transport

For investigation of the particle transport under various plasma conditions tracer impurities (aluminium) were injected into the plasma by laser blow-off technique avoiding perturbations of the global plasma parameters. The time behaviour of the Al-density was deduced from the line radiation of various ionization stages of Al by VUV and X-ray spectrometers and a soft X-ray camera system, respectively, providing the total radiation of H- and He-like Al. The transport parameters characterized by the diffusion coefficient D, the convection velocity v and the Al confinement time τ_{Al} are derived from simulating the measurements by the impurity transport codes STRAHL (Behringer,1987) and SITAR (WVII-A Team,1985).

Al Confinement Time Studies in ECRF Plasmas. In contrast to NBI-heated plasmas which mostly require a transport analysis with time dependent input profiles (SITAR) ECRF-heated plasmas were generally possible under quasi-stationary discharge conditions.

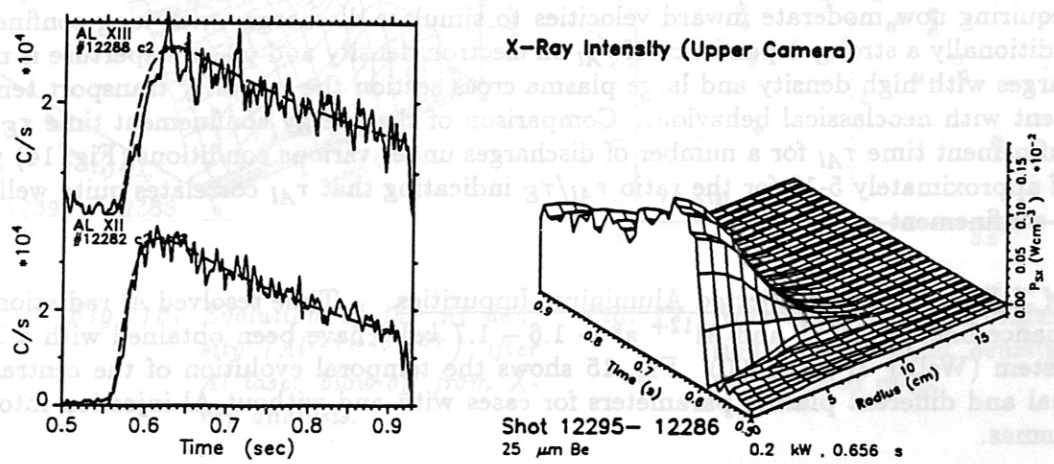

Fig. 13. Time development of Al-radiation after laser-blow-off at 550 ms: Line radiation of He- and H-like Al (left, broken lines: simulation by STRAHL with $D \simeq 0.08\,m^2/s$ and $\tau = 340\,ms$). Al-radiation seen by soft-X cameras (right).

In this case the temporal evolution of the measured radiation intensities was fitted with STRAHL using proper values of the diffusion coefficients D (assumed constant over radius for all ionization stages) and of the (radially increasing) convection velocity v. From these calculations also the

confinement time τ_{Al} was obtained.

Before wall conditioning in ECRF-experiments with $B = 2.5\ T$ typical diffusion coefficients of $D \simeq 0.1 - 0.2\,m^2/s$ and confinement times of $\tau_{Al} \simeq 40 - 70\,ms$ have been observed - roughly a factor of 4 lower transport and better confinement compared to experiments with half the magnetic field (corresponding to the particle confinement, (Ringler, 1990)). Reasonable fits could also be obtained omitting the convection velocity in the transport calculations leading to only 20% lower values for D.

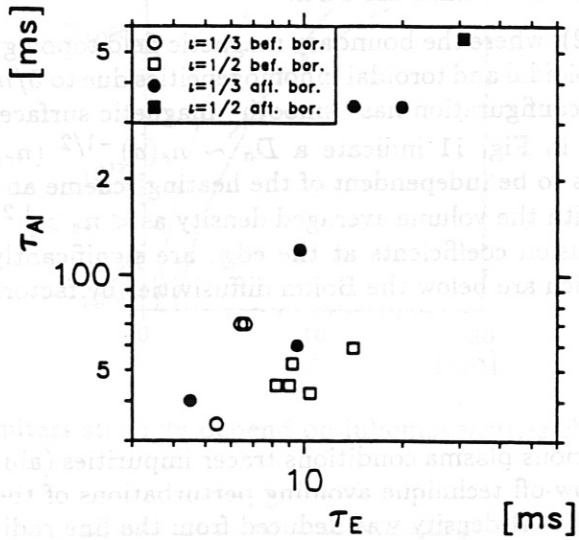

Fig. 14. Relation between τ_{Al} and the energy confinement time τ_E for ECRF plasmas (2.5 T).

Within the error bars no clear dependence of D and τ_{Al} on rotational transform and ECRF input power could be identified whereas the Al confinement time turns out to be a distinct function of the plasma aperture (approximately $\propto a^2$) while D remains nearly constant.

After boronization discharge conditions were achieved ($n_e \simeq 3.6{-}4.8{\cdot}10^{19}\ m^{-3}$, $a = 0.16{-}0.18\ m$) leading to Al confinement times up to 500 ms for ECRF input powers of 170 kW and 350 kW at $\iota \simeq 1/3$ (Fig. 13) and even larger values for $\iota \simeq 1/2$. The peaked radiation profiles (Fig. 13, right) are mainly due to the peaked temperature profile. Diffusion coefficients of $0.05 - 0.11\,m^2/s$ were derived requiring now moderate inward velocities to simulate discharges with long confinement times. Additionally a strong dependence of τ_{Al} on electron density and plasma aperture is noted. For discharges with high density and large plasma cross section the impurity transport tends to be consistent with neoclassical behaviour. Comparison of the energy confinement time τ_E with the Al confinement time τ_{Al} for a number of discharges under various conditions (Fig. 14) yields a factor of approximately 5-12 for the ratio τ_{Al}/τ_E indicating that τ_{Al} correlates quite well with the global confinement properties.

Analysis of X-Ray Profiles of Injected Aluminium Impurities. Time resolved Al radiation profiles (resonance lines of Al^{11+} and Al^{12+} at $\sim 1.6 - 1.7\ keV$) have been obtained with a X-ray camera system (Weller *et al.*, 1990). Fig. 15 shows the temporal evolution of the central soft X-ray signal and different plasma parameters for cases with and without Al injection into NBI heated plasmas.

The background corrected profiles can be either used for comparisons with transport simulations (see next section) or for a direct determination of the transport coefficients from the derived Al density profiles. This method (Pasini *et al.*,1990) can be applied, if the observed Al radiation profiles do not depend on the radial transport themselves and therefore the Al radiation coefficient ϵ (including effect of filter transmission) can be calculated in coronal equilibrium approximation (by IONEQ). This assumption could be verified for the particular plasma parameters by calculations with and without radial transport. Then the density of Al in the stages $A^{11+,12+,13+}$ (n_{AL})

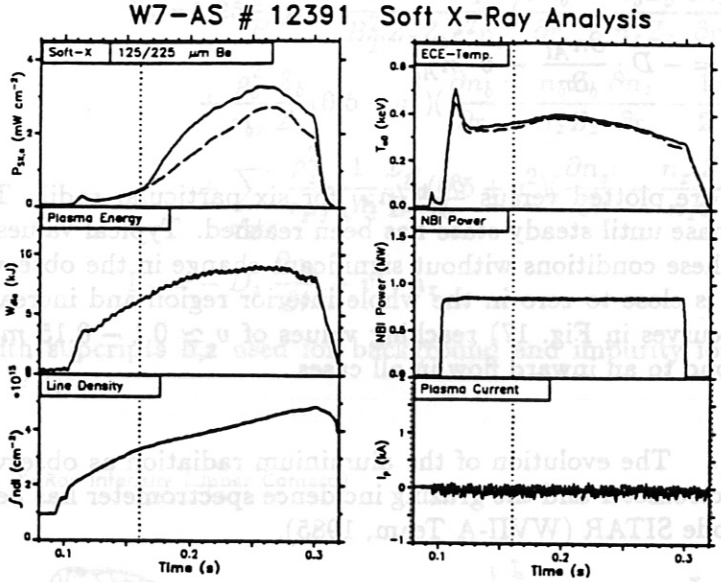

Fig. 15. X-ray signals and global plasma parameters for NBI heating at $B = 2.5\,T$, $\iota = 0.53$. Injection of aluminium in shot 12391 (solid lines) at marked time.

follows from

$$P_{Al}^{rad}(r,t) = n_{Al}(r,t) \cdot n_e(r,t) \cdot \epsilon(T_e(r,t)) \qquad (1)$$

Measured profiles of T_e and n_e from Thomson scattering are used in the calculations.

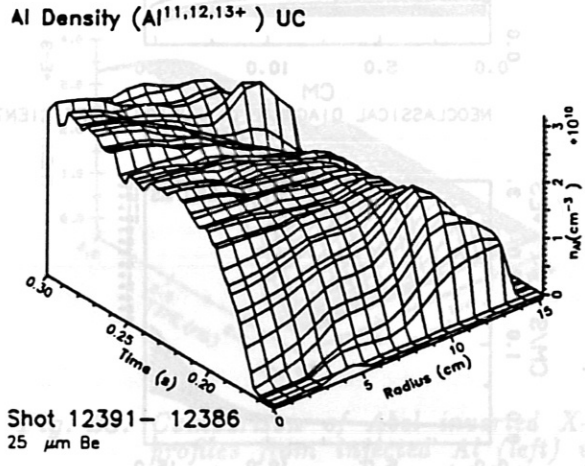

Fig. 16. Evolution of the Al density ($Al^{11+,12+,13+}$) after Al laser blow-off from X-ray analysis.

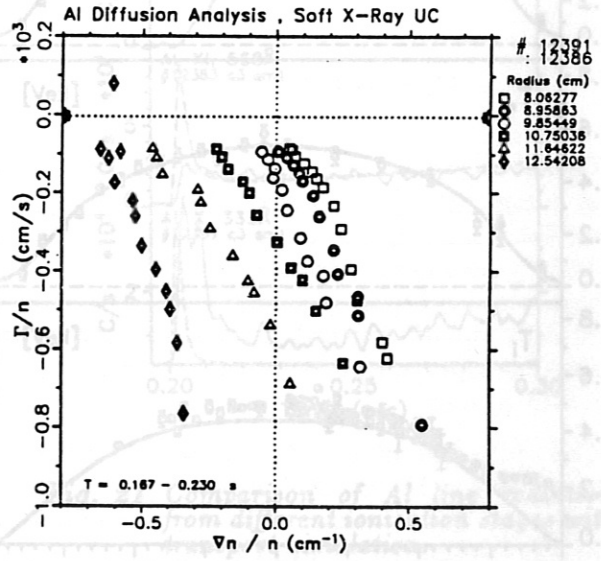

Fig. 17. Normalized transport fluxes as function of normalized density gradient for different radii.

For the NBI case referring to Fig. 15 the resulting density n_{Al} is given in Fig. 16. Just after Al ablation the Al density evolves through hollow profiles with subsequent central density buildup. Then the profiles remain peaked without showing any decay within the time of the discharge.

Neglecting source and sink terms the diffusion equation

$$\frac{\partial n_{Al}}{\partial t} = -\frac{1}{r}\frac{\partial}{\partial r}(r \cdot \Gamma_{Al}) \quad \Rightarrow \quad \Gamma_{Al}(r,t) = \frac{1}{r}\int_0^r \frac{\partial n_{Al}}{\partial t}(\rho) \cdot \rho \, d\rho \qquad (2)$$

is used to derive the transport flux Γ_{Al} with the usual ansatz

$$\Gamma_{Al} = -D \cdot \frac{\partial n_{Al}}{\partial r} - v \cdot n_{Al} \tag{3}$$

In Fig. 17 normalized fluxes Γ_{Al}/n_{Al} are plotted versus $\frac{\partial n_{Al}}{\partial r}/n_{Al}$ for six particular radii. The time interval covers the penetration phase until steady state has been reached. Typical values of $D \simeq 0.1 - 0.2\ m^2/s$ are obtained for these conditions without significant change in the observed radial range. The convection velocity is close to zero in the whole interior region and increases towards the outside (displacement of curves in Fig. 17) reaching values of $v \simeq 0.1 - 0.15\ m/s$. The sign of $v(r)$ was found to correspond to an inward flow in all cases.

Modelling with Neoclassical Transport. The evolution of the aluminium radiation as observed with the X-ray cameras, the Bragg spectrometer and the grazing incidence spectrometer has been simulated by the impurity transport code SITAR (WVII-A Team, 1985).

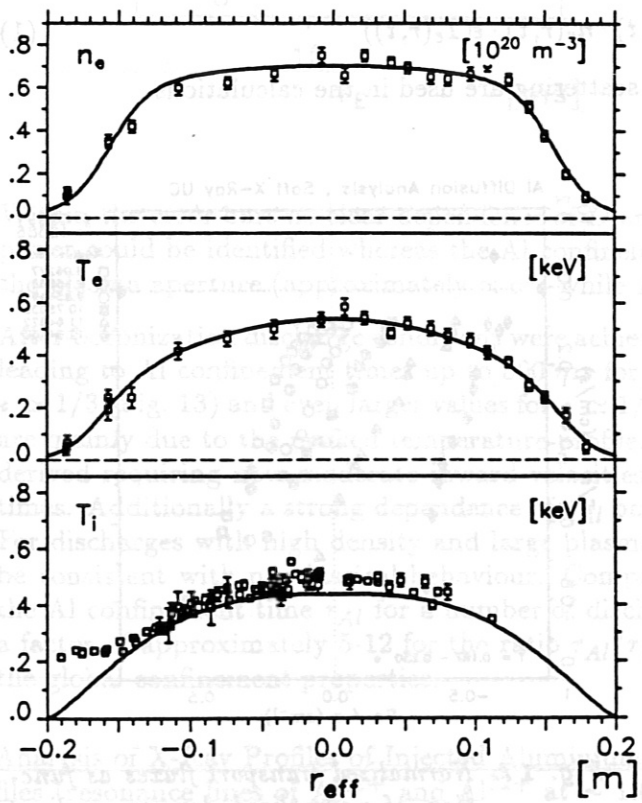

Fig. 18. Measured Profiles of n_e, T_e and T_i for NBI heating at $B = 2.5T$, $\epsilon = 0.53$ used as input for SITAR.

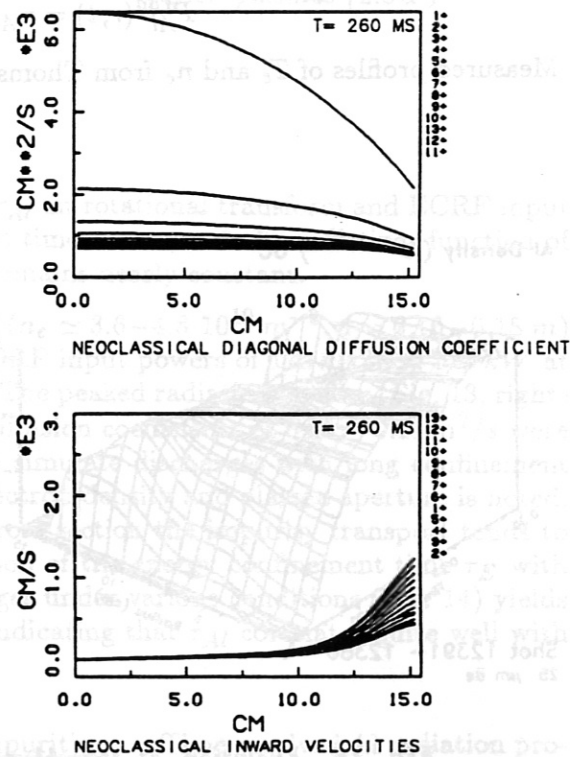

Fig. 19. Calculated Profiles of $D(r)$ and $v(r)$ according to given neoclassical expressions for different Al charge states.

Radial profiles of T_e, T_i and n_e are required as input for the code. Neoclassical transport fluxes (classical (CL), Pfirsch-Schlüter (PS) and banana-plateau (BP)) are used in the usual form derived for axisymmetric devices (tokamaks) with extensions to include effects of collisions between test impurities (Al) in different ionisation stages and between test impurities and a light impurity

background (C,O), respectively:

$$\Gamma_z = 1.25\frac{q}{R}\sqrt{m_z}\,\frac{T^{3/2}c^2 n_z}{B_T^2 Z_z Z_b e^2 n_b}\left(\frac{\partial n_b}{\partial r} - \frac{n_b Z_b}{n_z Z_z}\frac{\partial n_z}{\partial r} + \frac{1.5 n_b}{T}\frac{\partial T}{\partial r}\right)$$
$$+ \frac{\rho_b^2}{\tau_{bz}}\frac{Z_b}{Z_z}(0.5+q^2)\left(\frac{\partial n_b}{\partial r} - \frac{n_b Z_b}{n_z Z_z}\frac{\partial n_z}{\partial r} - \frac{1}{2}\frac{n_b}{T}\frac{\partial T}{\partial r}\right) \qquad (4)$$
$$+ \sum_{z'\neq z}\frac{\rho_{z'}^2}{\tau_{z'z}}\frac{1}{\sqrt{2}}\frac{Z_{z'}}{Z_z}(0.5+q^2)\left(\frac{\partial n_{z'}}{\partial r} - \frac{n_{z'}Z_{z'}}{n_z Z_z}\frac{\partial n_z}{\partial r} - \frac{1}{4}\left(\frac{Z_{z'}}{Z_z}-1\right)\frac{n_{z'}}{T}\frac{\partial T}{\partial r}\right)$$

$$\Gamma_z = -D_z\frac{\partial n_z}{\partial r} - v_z \cdot n_z$$

with supcripts b,z used for background and impurity ions, ρ Larmor radius, τ collision time, $T = T_i$.

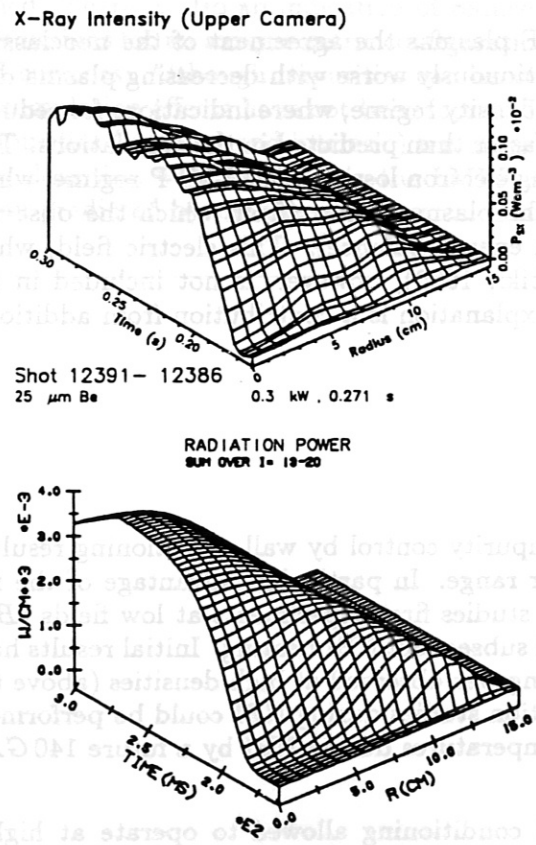

Fig. 20. Comparison of Abel inverted X-ray profiles from injected Al (left) with transport simulation (right). NBI heating at $B = 2.5\,T$, $\iota = 0.53$.

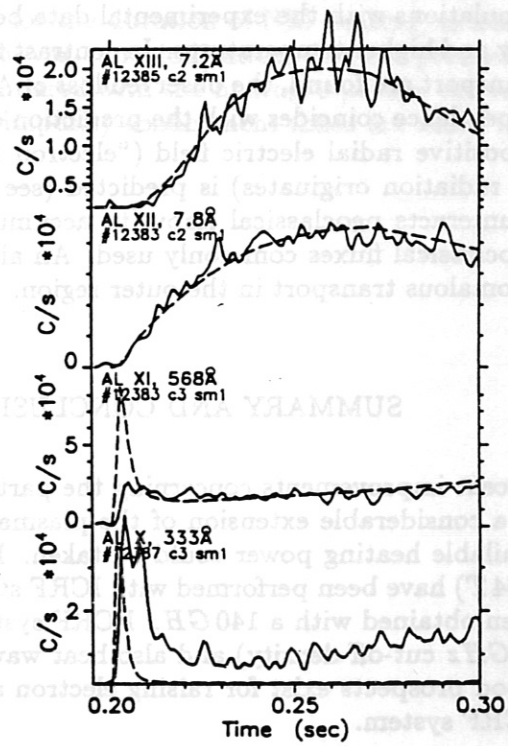

Fig. 21 Comparison of Al line radiation from different ionisation stages with transport simulation.

Typically the PS fluxes for Al are the most important with background ions (H,D) in the BP regime and light impurities (C,O) already in the PS regime. For the moderately drift optimized stellarator W7-AS by a factor of ~ 2 reduced PS currents are predicted (Wobig, 1991) in accordance with measurements of the Shafranov shift (Renner, 1990). The PS transport flux is expected to be reduced by the same amount because of the lower PS factor compared with tokamaks or conventional stellarators ($\sim 2q^2$, $q = 1/\iota$). Therefore muliplicators < 1 were frequently used in the simulations if the neoclassical fluxes according to (4) gave too high values and the predicted rise of the central Al radiation was faster than observed. Another essential modification with respect to expression (4), however, had to be used in almost all cases investigated. In the PS regime "temperature screening" is expected due to the temperature gradient. Since the background density is typically rather flat in the interior region (Fig. 18), the ∇T term can

lead to broader impurity profiles and faster loss of impurities, which was found to be inconsistent with the experimental data. In particular, in the quasi-stationary phase Al density profiles are required, which are more peaked than the background plasma. This is also in accordance with initial measurements of moderately peaked Z_{eff} profiles from intrinsic impurities (C,O,Ti) from visible bremsstrahlung analysis. Best agreement was found by omitting the ∇T term. This approach is justified, because the friction with light impurities dominates, for which the ∇T is predicted to have less influence or even reverses sign depending on collisionality and the impurity density (Hirshman, 1981). Referring to the same plasma conditions ($P_{NBI} = 0.8\,MW$, $B = 2.5\,T$, $\iota = 0.53$) as discussed in the previous section (Figs. 15,16,17) the neoclassical values of $D(r)$ and $v(r)$ are calculated (Fig. 19) from the corresponding measured input profiles, which are given in Fig. 18. Good agreement of the predicted transport coefficients with the experimentally derived values (from Fig. 17) is obtained. The result of simulating the Al radiation by the SITAR code is shown in Figs. 20,21. The essential features seen in the Abel inverted X-ray emission of aluminium after the injection of Al are reproduced quite well by the calculations with neoclassical transport. Under these experimental conditions the background particle transport was also found close to the predictions of neoclassical transport.

Concerning the Al transport investigations in ECRF plasmas the agreement of the neoclassical simulations with the experimental data becomes continuously worse with decreasing plasma density and higher temperatures. In contrast to the high density regime, where indications for reduced transport are found, the observed loss of Al is much faster than predicted in the simulations. This dependence coincides with the prediction of increasing electron losses in the LMFP regime, where a positive radial electric field ("electron root") in the plasma center (from which the observed Al radiation originates) is predicted (see section on energy balance). This electric field, which counteracts neoclassical impurity accumulation (Obiki, 1989), however, is not included in the neoclassical fluxes commonly used. An alternative explanation is a contribution from additional anomalous transport in the outer region.

SUMMARY AND CONCLUSIONS

Recent improvements concerning the particle and impurity control by wall conditioning resulted in a considerable extension of the plasma parameter range. In particular, advantage of the full available heating power could be taken. For high β studies first experiments at low fields ($B = 0.64\,T$) have been performed with ICRF start-up and subsequent NBI heating. Initial results have been obtained with a $140\,GHz$ ECRF system. Heating was observed at high densities (above the $70\,GHz$ cut-off density) and also heat wave propagation studies during NBI could be performed. Good prospects exist for raising electron and ion temperatures during NBI by a future $140\,GHz$ ECRF system.

The reduction of low Z and Fe impurities by wall conditioning allowed to operate at higher densities (up to cut-off limit during ECRF), reaching $\sim 3 \cdot 10^{20}\ m^{-3}$ and $< \beta > \sim 1\%$ with NBI. However, the titanium radiation can still affect the power balance significantly. This problem will be eliminated by using boron-graphite compounds as limiter and shield material in the next experimental campaign.

The global energy confinement (maximum confinement time $\sim 35\,ms$) can be well described, independently of the heating method, by the Lackner-Gottardi scaling relation in the whole parameter range. The benefit of a high rotational transform could not fully be demonstrated due to the reduced plasma cross section and increased impurity problems caused by plasma wall contacts outside the separatrix. Therefore, additional efforts are necessary to control the recycling and the impurity release by pumped divertor/limiter components.

Local energy balance and heat wave propagation studies show, that the electron heat conductivity in the low density regime exceeds the neoclassical values significantly. Only at lowest collisionalities (LMFP regime) the neoclassical values are comparable with the values derived from the experimental data. The ion heat conduction, which is the dominant loss channel at higher densities, is in the range of neoclassical predictions, if the reduction by the ambipolar radial electric

field is taken into account (except for very high densities). The reduction of the ion transport, however, is less pronounced in W7-AS compared with W7-A, since losses of fast injected particles are negligible due to tangential beam injection.

The particle transport is analyzed by taking into account the 3-dimensional distribution of the ion sources in the DEGAS code. A comparison of the particle fluxes, as resulting from the H_α calibrated code simulations, with the neoclassical predictions (including E_r) shows a reasonable agreement in the bulk plasma for both ECRF and NBI discharges. At very high densities (NBI) the consistency with neoclassical fluxes extend up to the boundary. The diffusion coefficient at the edge depends on the edge density as $D_a \sim n_e(a)^{-1/2}$, which seems to be independent of the heating method and limiter aperture.

Impurity confinement times deduced from laser blow-off experiments are typically much longer compared with the energy confinement time (typically a factor of ~ 10 for Al-injection in ECRF discharges). At high densities, particularly during NBI, the experimental data are reasonably well simulated with neoclassical transport fluxes. However, "temperature screening" effects, as predicted for the Pfirsch-Schlüter (PS) diffusion under particular conditions, could not be identified. There is also an indication of reduced transport in the plasma center, compared with the predictions for an axisymmetric configuration. This is expected for W7-AS because of the reduced PS currents. Although impurities can be well confined for the duration of NBI heating, extreme accumulation effects have not been found. There is, however, some indication, that the profiles of impurities (injected and intrinsic) are more peaked compared with the hydrogen profile. At very low densities, with electrons in the LMFP regime, the impurity confinement times are much less than predicted by the used neoclassical model.

REFERENCES

Afanasjev, V.I., Izvozchikov, A.B., Junker, J. *et al.*(1991). *Proc. 18th Euro. Conf. on Contr. Fusion and Plasma Phys.,* Berlin, 1991, 15C (2),209-212.

Behringer, K. (1987). Description of the Impurity Transport Code "STRAHL", *JET-R-(87)*08.

Brakel, R., Burhenn, R. *et al.*(1991). *Proc. 18th Euro. Conf. on Contr. Fusion and Plasma Phys.,* Berlin, 1991, 15C (2), 189-192.

Grigull, P. *et al.*(1990). *J. Nucl. Mater.,* 176&177, 975-982.

Hartfuß , H.J. *et al.*(1986). Nuclear Fusion 26, 678.

Hartfuß , H.J. *et al.*(1991). *Proc. 18th Euro. Conf. on Contr. Fusion and Plasma Phys.,* Berlin, 1991, 15C(2), 213-216.

Heifetz, D.B. *et al.* (1982). *J. Comput. Phys.,* 46, 309.

Hirshman, S.P., Sigmar, D.J. (1981) *Nuclear Fusion* 21, 1079.

Lackner, K., Gottardi, N.A.O. (1990) *Nuclear Fusion* 30, 767.

Lazaros, A. *et al.*(1991). *Proc. 18th Euro. Conf. on Contr. Fusion and Plasma Phys.,* Berlin, 1991, 15C (2), 197-200.

Lister, G.G. *et al.*(1983). *Proc. 11th Euro. Conf. on Contr. Fusion and Plasma Phys.,* Aachen, 1983, 7D (2), 323.

Obiki, T. *et al.*(1989). *in Plasma Physics and Controlled Nuclear Fusion Research 1988 (Proc. 12th Int. Conf. Nice, 1988),* 2, IAEA, Vienna (1989) 337-348.

Pasini, D., Weisen, H., Weller, A., Edwards, A.W. (1990). Measurement of Impurity Concentrations and Z_{eff} in JET Using X-ray Tomography, *Bull. Am. Phys. Soc.* 35, 1998.

Penningsfeld, F.-P. *et al.*(1991). *Proc. 18th Euro. Conf. on Contr. Fusion and Plasma Phys.,* Berlin, 1991, 15C (2), 201-204.

Philipps, V., *et al.* (1989). *Plasma Physics and Controlled Fusion,* 31, 1685-1698.

Rau, F. *et al.*(1990). *Proc. 17th Euro. Conf. on Contr. Fusion and Plasma Phys.,* Amsterdam, 1990, 14B(2), 517.

Renner, H. *et al.*(1989). *Proc. 16th Euro. Conf. on Contr. Fusion and Plasma Phys.,* Venice, 1989, 1579-1596

Renner, H., Gasparino, U., Maaßberg, H., Kühner, G., Ringler, H., Sardei, F., Weller, A., W7-AS Team, NBI Group, Pellet Injection Group, ECRH Team (1990). Confinement Properties of the "Advanced Stellarator" WENDELSTEIN 7-AS. *Plasma Physics and Controlled Nuclear Fusion Research 1990* (Proc. 13th Int. Conf. Washington, DC, 1990), IAEA-CN-53/C-1-2.

van Rij, W.I. and Hirshmann, S.P. (1989), *Phys. Fluids B,* 1, 563.

Ringler, H., Gasparino, U., Kühner, G., Maaßberg, H., Renner, H., Sardei, F., W7-AS Team, NBI Team, ECRH Group (1990). Confinement Studies on the WENDELSTEIN 7-AS Stellarator. *Plasma Physics and Controlled Fusion,* 32, 933-948.

Sardei, F. *et al.*(1990). *Proc. 17th Euro. Conf. on Contr. Fusion and Plasma Phys.,* Amsterdam, 1990, 14B(2), 471.

Sardei, F. *et al.*(1991). *Proc. 18th Euro. Conf. on Contr. Fusion and Plasma Phys.,* Berlin, 1991, 15C (2), 193-196.

Schneider, U. *et al.*(1990). *J. Nucl. Mater.,* 176&177, 350-356.

Stangeby P.C. and McCracken,G.M. (1990). Nuclear Fusion 30, 1225.

Weller, A. *et al.*(1987). Modelling of Soft X - Ray emission from JET plasmas, JET Joint Undertaking internal Report *JET-IR-(87)*10.

Weller, A. *et al.*(1990). *Proc. 17th Euro. Conf. on Contr. Fusion and Plasma Phys.,* Amsterdam, 1990, 14B(2), 479.

Winter, J. *et al.*(1989). *J. Nucl. Mater.,* 162-164, 713-723.

Wobig, H., *et al.*(1987). *Plasma Physics and Controlled Nuclear Fusion Research 1986* (Proc. 11th Int. Conf. Kyoto, 1986), 2, IAEA, Vienna (1987) 369.

Wobig, H. (1991). *Proc. 18th Euro. Conf. on Contr. Fusion and Plasma Phys.,* Berlin, 1991, 15C (4), 213-216.

WVII-A Team, NI-Group (1985) *Nuclear Fusion* 25, 1593.

ION HEAT CONDUCTIVITY, RADIAL ELECTRIC FIELDS AND CX-LOSSES IN THE W7-AS STELLARATOR

V.I. Afanasjev*, A.B. Izvozchikov*, J. Junker, M. Kick, H. Maaßberg,
W. Ohlendorf, F. Sardei, S. Zöpfel, W7-AS Team and NBI Team
Max-Planck Institut für Plasmaphysik
Association EURATOM-IPP, D-8046 Garching, Germany
*) A.F.Ioffe Physical-Technical Institute, Leningrad, USSR
ECRH Group
Institut für Plasmaforschung der Universität Stuttgart
D-7000 Stuttgart, Germany

Introduction

The energy balance analysis for both ECR (up to 1 MW at 70 GHz) and NBI (up to 1.6 MW with tangential injection) heated discharges in the Wendelstein 7-AS stellarator ($B < 3$ T, $R = 2$ m, $a < 18$ cm, 5 field periods) is based on measured profiles: electron density and temperature by Thomson scattering, ion temperature by active CX neutral particle analysis as well as by CXRS (CX recombination spectroscopy). Full T_i profiles are provided by a charge-exchange diagnostic setup consisting of a diagnostic neutral beam injector and four neutral particle analyzers. The D_0-fluxes originating from the H_0-beam are detected tangentially. Lifting the analyzers allows to scan the plasma cross section vertically from $-a$ to $a/2$. The position along the diagnostic neutral beam in real space is transformed to the effective plasma radius, r (magnetic co-ordinate). The spatial resolution, Δr, is about ± 1 cm. This transform depending on the rotational transform, the plasma pressure and an additional vertical field is also applied to the Thomson diagnostic data leading to symmetric n_e, T_e and T_i profiles in the effective plasma radius, r.

The experimental estimate of the local T_i is higher than the real value for higher densities due to the attenuation of the outgoing neutral flux. A standard procedure /1/ is used for correction of the T_i profile. For the NBI heated discharge of Fig. 3, the resultant T_i profile (broken line) deviates in the central part from the uncorrected data (full dots). For the ECRH discharge with lower density in Fig. 1 the correction is small. The "non-Maxwellian" part in the outer range ($r > 15$ cm) of the T_i profiles is disregarded for the energy balance analysis. Only few T_i data are measured by the CXRS diagnostic up to now with reasonable agreement with the CX temperatures. Furthermore, the Doppler shift of the background impurity lines of O and C excited by the diagnostic beam can be used to estimate the poloidal rotation velocity. An accurate evaluation of the diamagnetic drift component, however, is necessary to obtain the radial electric field. A first analysis indicates rather small values of the radial electric field for both ECRH and NBI discharges.

Energy Balance Analysis

For the discharges discussed in this paper the electron and ion energy balance are analyzed independently. This procedure becomes critical at higher densities where the collisional coupling of electrons and ions, determined by the absolute difference of $T_e(r)$ and $T_i(r)$, dominates the energy balance. At even higher densities ($n_e > 10^{14}$ cm^{-3}), where the electron and ion temperatures are nearly identical, the total energy balance in which the electron-ion coupling disappears can be considered.

The ECR power deposition which is highly localized close to the resonance zone is modelled analytically corresponding to 3D ray tracing calculations /2/. For fundamental heating (o-mode at $B \simeq 2.5$ T), very high single pass absorption ($> 70\,\%$) is found for

$T_e > 1$ keV. The NBI electron and ion heating profiles are calculated by the FAFNER code (3D Monte-Carlo code) /3/. For the tangential injection in W7-AS with high beam absorption the fast ion orbit losses are very small and the effect of a radial electric field which is omitted in the computations up to now is expected to be of minor importance for the power deposition profiles. Furthermore, the reduction of NBI heating efficiency due to fast CX losses is negligible in the bulk part of the plasma which is consistent with DEGAS simulations of the neutral gas profiles. The full 3D DEGAS code /4/ is used to simulate the neutral gas densities and fluxes in the complex topology of W7-AS with all main contributions to the particle sources included /5/. DEGAS calculates also the thermal CX losses which are relevant for the ion energy balance. For NBI discharges at higher densities the CX losses turn out to be rather small compared to the ion transport losses in the bulk part of the plasma. In ECRH discharges at lower densities, however, where the collisional ion heating is rather small the ion energy balance is significantly affected by the CX losses.

As impurity concentration and Z_{eff} profiles are not available at present, a mean Z_{eff} is roughly estimated for moderate and higher densities by comparing the kinetic energies evaluated from the profiles with the total energy content measured by the diamagnetic loop. C, O and Fe (simulating also Ti) are used for modelling the impurity concentrations. On this basis the radiation loss profile (normalized to bolometry and SX data) as well as the collisional electron-ion power transfer, P_{ei}, are calculated. The electron energy balance is solved with a purely diffusive ansatz for the electron heat conduction. The resultant electron heat conductivity, $\chi_e{}^{\text{exp}}$, is found to be much larger than the neoclassical predictions (based on DKES code) /6/. Only for high T_e (> 1.5 keV) at low density the neoclassical χ_e exceeds the experimental one. The ion transport losses are determined by the direct ion heating in NBI discharges, the collisional heating, P_{ei}, and the CX losses, P_{CX}, and are compared with the neoclassical predictions.

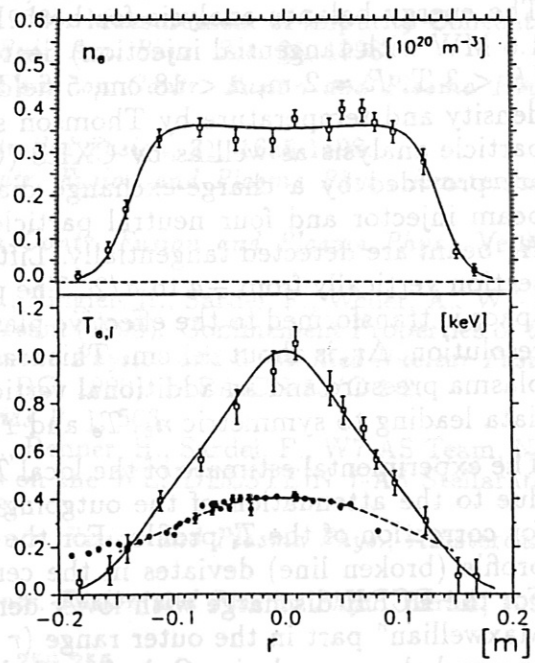

Fig. 1: *ECRH discharges with 140 kW input power (shots 12314-32): n_e (upper plot), T_e (open squares) and T_i (full dots) data and fit curves.*

The mono-energetic DKES code /7/ is used to calculate the neoclassical transport properties. With energy convolution included, the full transport matrix for each plasma species depends on collisionality and radial electric field. The condition of ambipolarity of all particle fluxes is used for calculating the radial electric field. At present, only one ion species is taken into account. For the discharges of Figs. 1 and 3, only the ion root with $E_r < 0$ exists. The E_r values are up to -100 V/cm and thus have a very small effect on the electron transport coefficients. The ion transport coefficients, however, are significantly reduced (up to a factor of 3, χ_i even more), the radial electric fields correspond to $e\Phi \approx kT_i$. In this approach with only one ion species the E_r values are rather insensitive to Z_{eff}. Non-thermal ions in case of NBI heating can increase the radial electric field although this effect is small for tangential injection and the fast beam ion density is of the order of only a few percent of the ion density.

Ion Energy Balance

In ECRH discharges, optimum energy confinement is found at higher densities for low heating power level /6/. An example with ECR input power of about 140 kW and $\tau_E \approx 35$ ms is shown in Fig. 1. Note the nearly constant T_e gradient which is typical for good electron energy confinement. The electron heat conduction at outer radii is rather small, radiative power loss ($\approx$ 40 kW) and strong collisional power transfer (P_{ei} up to 90 kW) dominate. At r = 8 cm, $\chi_e{}^{exp}$ is a factor of 5 larger than the neoclassical prediction. The ion energy balance is shown in Fig. 2. Here, the neoclassical energy loss with $E_r = 0$ (thin broken line) reaches 250 kW which is more than the total input power. The neoclassical energy flux with the ambipolar E_r included (thick broken line) is smaller than the available power (dotted line) given by $P_{ei} - P_{CX}$. Note that P_{ei} depends on the profiles of the impurity concentrations, a mean $Z_{eff} \approx 2$ was assumed for this case. However, an additional ion energy loss term increasing with radius is necessary to fulfill the ion energy balance. These results are also found for ECRH discharges at lower densities where P_{ei} is smaller but P_{CX} is increased.

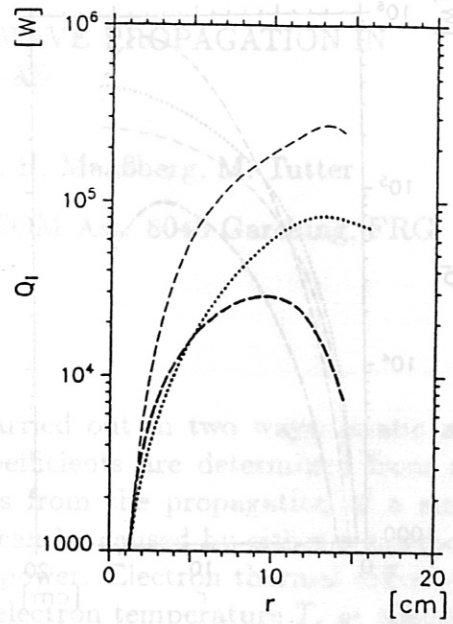

Fig. 2: *Ion energy balance for the ECRH discharges of Fig. 1: available power, $P_{ei} - P_{CX}$ (dotted line), the neoclassical predictions with $E_r = 0$ (thin broken line) and with ambipolar E_r (thick broken line).*

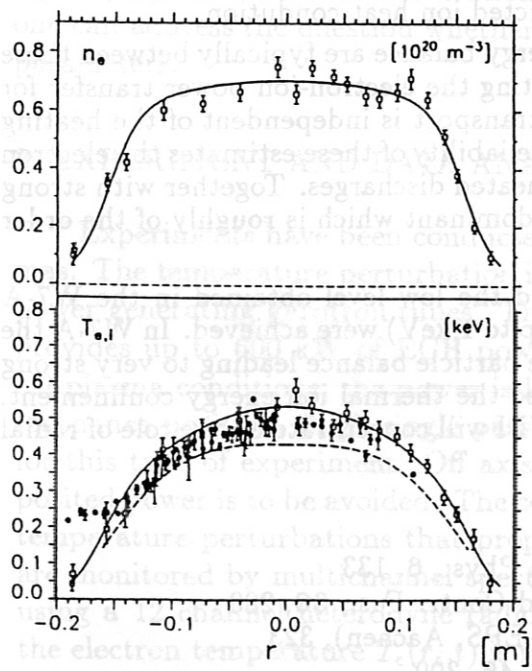

Fig. 3: *NBI discharges with 700 kW input power (shots 12366-89): n_e (upper plot), T_e (open squares) and T_i (full dots) data and fit curves.*

For the NBI discharge ($P_{NBI} \approx$ 700 kW) at medium density in Fig. 3 (n_e up to $3 \cdot 10^{14}$ cm^{-3} was obtained in NBI discharges) the T_i correction of the direct CX data (full dots) turned out to be rather small (< 10 %), but the effect on the electron-ion power transfer is significant: P_{ei} = 180 kW ±40 kW. The rather large error in the experimental temperature difference affects significantly the electron energy balance leading to about 50 % uncertainty in electron heat conduction at outer radii. P_{ei} adds to the ion heating by the NBI (thin dot-dashed curve in Fig. 4). The available power for ion energy transport, $P_{NBI} + P_{ei} - P_{CX}$ (dotted line), is again between the neoclassical prediction with E_r = 0 (thin broken line) and with the ambipolar electric field included (thick broken line). In this discharge, CX losses play only a minor role, the NBI ion heating is larger than the electron-ion power transfer. An additional ion heat loss with respect to the ambipolar neoclassical prediction increasing with r is necessary.

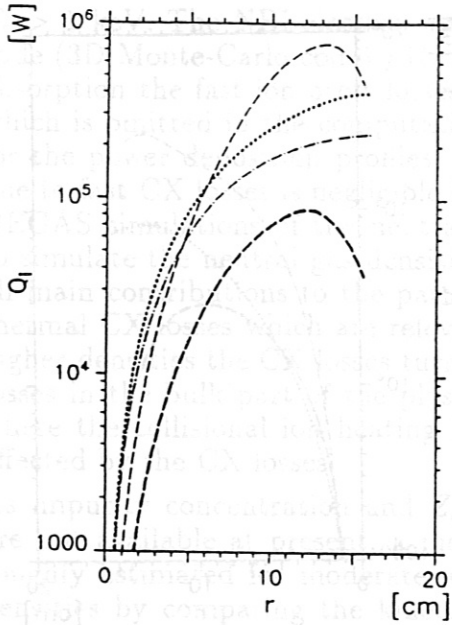

Fig. 4: *Ion energy balance for the NBI discharges of Fig. 3: NBI ion heating, P_h^i (dot-dashed line), total available power, $P_h^i + P_{ei} - P_{CX}$ (dotted line), the neoclassical predictions with $E_r = 0$ (thin broken line) and with ambipolar E_r (thick broken line).*

Also for a combined discharge with 400 kW NBI and 350 kW ECR heating power at moderate densities ($n_e(0) = 4.2 \cdot 10^{13}$ cm^{-3}, ECF power deposition about 7 cm off-axis, $T_i(0) \approx 700$ eV), the ion energy transport lies between the neoclassical predictions with and without ambipolar electric field included.

Conclusions

The radial electric fields calculated by the condition of ambipolarity of the neoclassical particle fluxes (with only one ion species included) turned out to be rather small which is consistent with first observations of the Doppler shift of impurity lines (CXRS). The particle fluxes simulated by DEGAS code agree reasonably well with the neoclassical predictions in the bulk part of the plasma /5/. As in cases with the ion root ($E_r < 0$) the ambipolar fluxes are mainly determined by the electrons, the discrepancy between experimental and neoclassical electron heat conduction plays a minor role for the reliability of the radial electric field estimation. More sensitive for the E_r estimation is the use of only one ion species in the ambipolarity condition. Including the radial electric field in the neoclassical models results in an already significant reduction of the predicted ion heat condution.

The experimental values obtained from the ion energy balance are typically between these two theoretical cases. Within the errors in estimating the electron-ion power transfer for moderate and higher densities, the electron heat transport is independent of the heating method (ECRH, NBI and combined). Within the reliability of these estimates the electron heat transport plays only a minor role in the NBI heated discharges. Together with strong radiative power losses the ion energy transport is dominant which is roughly of the order of the neoclassical prediction.

The ion transport on W7-AS has not yet reached the low level obtained in the W7-A stellarator where much higher ion temperatures (up to 1 keV) were achieved. In W7-A the nearly perpendicular NBI significantly affected the particle balance leading to very strong radial electric fields /8/ which essentially improved the thermal ion energy confinement. Further investigations in W7-AS with tangential NBI will concentrate on the role of radial electric field on the confinement properties.

References

/1/ V.V. Afrosimov et al. (1980), Sov. J. Plasma Phys., **6**, 133
/2/ U. Gasparino et al. (1988), Plasma Phys. and Contr. Fus., **30**, 283
/3/ G.G. Lister et al. (1983), **ECA 7D-II** (11th EPS, Aachen), 323
/4/ D.B. Heifetz et al. (1982), J. Comput. Phys., **46**, 309
/5/ F. Sardei et al. (1991), this conference
/6/ H. Ringler et al. (1990), Plasma Phys. and Contr. Fus., **32**, 933
/7/ W.I. van Rij and S.P. Hirshman (1989), Phys. Fluids B, **1**, 563
/8/ H. Wobig et al. (1987), Plasma Phys. and Contr. Nucl. Fus. Res., **2**, 369

THERMAL DIFFUSIVITY FROM HEAT WAVE PROPAGATION IN WENDELSTEIN 7-AS

H.J. Hartfuß, V. Erckmann, L. Giannone, H. Maaßberg, M. Tutter

Max-Planck-Institut für Plasmaphysik, EURATOM Ass. 8046 Garching, FRG

1. INTRODUCTION

Electron thermal diffusivity studies can be carried out in two ways: static and dynamic. In the static analysis, the transport coefficients are determined from the stationary power balance, in the dynamic analysis from the propagation of a small perturbation of the stationary plasma state which can be caused by either a sawtooth generated heat pulse or modulation of the heating power. Electron thermal diffusivity χ_e is deduced from the evolution of the perturbed electron temperature T_e at different locations r_i in the plasma. χ_e values obtained from perturbation analysis are usually greater than those calculated from power balance [1,2,3]. It has been pointed out that there is a principal difference between static and perturbative analysis [4]. Whereas the static method yields the transport coefficient $\chi_e = q_e/n_e\nabla T_e$, the perturbative method leads to an increase of the flux q_e as a result of an increase in the temperature gradient ∇T_e. The quantity determined is an incremental χ_e as defined by $\chi_e^{inc} = \partial q_e/n_e\partial(\nabla T_e)$. By varying the modulation of the heating power at different frequencies and amplitudes one can address the question whether or not this discrepancy is a function of the varied parameters.

2. EXPERIMENT AND DATA ANALYSIS

Experiments have been conducted in purely electron cyclotron heated (ECH) plasmas. The temperature perturbation is introduced by the modulation of one of the ECH power generating gyrotron tubes. The ECH system installed at the W7-AS stellarator provides up to 600 kW of ECH power at 70 GHz in the ordinary mode. Under typical plasma conditions, the power is locally deposited within about 3 cm of the chosen resonance position. High single pass absorption is a necessary experimental condition for this type of experiment. Off axis power deposition in addition to the centrally deposited power is to be avoided. The central deposition of modulated ECH power induces temperature perturbations that propagate away radially from the plasma core. They are monitored by multichannel spectroscopy of the electron cyclotron emission (ECE) using a 12 channel heterodyne radiometer [5]. In this way the temporal evolution of the electron temperature $T_e(r_i,t)$ is measured at 12 different radii r_i, either on the high or the low field side of the plasma column. The perturbation amplitude and the time delay both as function of radius are the experimental quantities of interest. They are of the order of a few ten down to about 1 eV and a few ms respectively.

Numerical modelling of heat wave propagation is carried out by starting with the power

balance equation,

$$(3/2)\partial/\partial t(n_e T_e) + \vec{\nabla}.\vec{Q}_e = n_e T_e \vec{\nabla}.(\vec{\Gamma}_e/n_e) + S_x$$

with $\vec{Q}_e = -n_e \chi_e \vec{\nabla} T_e + (3/2) T_e \Gamma_e$. Because the induced perturbation in density $\tilde{n}_e$ and flux $\tilde{\Gamma}_e$ is small the linearized equation

$$\partial \tilde{T}_e/\partial t = (2/3n_{eo})[(1/r)\partial/\partial r(r n_e \chi_e \partial \tilde{T}_e/\partial r) + \tilde{S}_x]$$

is solved. $\tilde{S}_x = (3/2) n_e (\tilde{T}_i - \tilde{T}_e)/\tau_{ei}$, is the ion-electron exchange term, τ_{ei} being the collision time. The most inner temperature channel located outside the power deposition zone is used as the forced boundary condition [6]. The electron thermal diffusivity is determined by fitting the measured propagation delay with those predicted using a given $\chi_e(r)$. In this formalism the electron-ion term is retained but density perturbations are not considered as measurements show that they are very much smaller than the temperature perturbations.

Figure 1. shows the propagation delay as a function of radial position as measured for different modulation frequencies, f = 23, 69, 138 Hz. The amplitude of the power modulation is held constant at 20 kW. The other plasma parameters are as follows: total ECH power 130 kW, central electron density $4.5 \text{x} 10^{19}/m^3$, edge value of the rotational transform 0.34, and central electron temperature 600 eV. Although the modulation amplitude is constant, the temperature modulation is a function of modulation frequency. The feature that at the outer radii the propagation delay apparently goes to zero for those two experiments at the higher modulation frequency is caused by a decrease in coherence between the temperature perturbation and the applied modulation. At the lower frequency, for which the temperature perturbation decay is longer, the coherence improves and the time delay can accurately be determined. These problems do not affect the time delay measurements of the inner channels where the perturbation is of sufficient amplitude to provide reliable measurements of the time delay. Using the inner channels only, the trend can be deduced that a decrease of modulation frequency leads to lower values of the deduced χ_e.

A complementary scan in the amplitude of the perturbations at f = 23 Hz and f = 69 Hz was carried out too as the scan at constant level of power modulation yields perturbations with greater amplitude at lower frequency. With increasing modulation amplitude changes in the plasma parameters are non-negligible. But again, for comparable average deposited power, the χ_e values deduced decrease with decreasing modulation frequency. As shown in fig. 2, only a small variation of the time delay as function of plasma radius is observed for 23 Hz modulation frequency, even in those cases where the perturbation was increased by a factor of 4. At 69 Hz the time delay in the three outermost channels decreases as the amplitude of the modulation increases by a factor of 3. In this case the feature cannot be explained by a loss of coherence of perturbation and modulation signal because coherence increases with increasing modulation amplitude. The observation may be explained by insufficient central power deposition leading to power deposition in the plasma edge. Such power deposition produces temperature perturbations that propagate inward destroying the monotonic time and amplitude evolution. Using only inner

channels where this process is no longer affecting the time delay measurements, it is found again that the deduced value of χ_e is independent of the perturbation amplitude.

3. DISCUSSION

The amplitude independence of the deduced value of χ_e at a given modulation frequency is particularly surprising. A temperature dependence or temperature gradient dependence of χ_e has been invoked as a possible reason for the difference between the χ_e values obtained from the dynamic and the static method. At the largest modulation amplitude, the relative temperature perturbation close to the plasma center is 10 per cent with a corresponding increase in the temperature gradient. A second important point is the result that in all cases analysed to date, the value of χ_e obtained by the perturbation analysis has not exceeded the static value by more than a factor of 2 for the lowest modulation frequency used.

The need for a heat pinch term in the conductive flux has been demonstrated in tokamaks [7]. Our results are consistent with the suggestion that the discrepancy between static and dynamic values of χ_e arises because of this heat pinch term. The amplitude variation in this case would be expected to yield a constant value of χ_e. The frequency dependence of the inferred value of χ_e would then have to arise because of the changes in the time scales involved as the modulation frequency was varied. This hypothesis will be tested in further experiments and analysis. The possibility that edge deposition plays a certain role cannot be ruled out at this time and it remains to be seen if this dependency continues to be found under experimental conditions where the optical depth and hence the power deposition at the resonance is higher. In addition, this hypothesis has to be reconciled with the observation of flat T_e profiles in off-axis ECH plasmas in stellarators which suggests that the heat pinch term may not be of importance.

4. CONCLUSION

Determination of the electron thermal diffusivity χ_e by heat wave propagation analysis was experimentally proven. The χ_e values obtained agree with the static value within a factor of 2 in contrast to the results from tokamak sawtooth propagation analysis. χ_e was found to be dependent on frequency and independent on amplitude, which seems to support the proposal for a heat pinch term in the conductive flux.

5. REFERENCES

[1] E. Frederickson, NF 26, 899 (1986)
[2] G. Jahns et al., NF 26, 226 (1986)
[3] H.J. Hartfuss et al., NF 26, 678 (1986)
[4] N.J. Lopes Cardozo et al., PPCF 32, 983 (1990)
[5] H.J. Hartfuss et al., Proc. EC6, p. 281-290, Oxford, 16.-17.9. (1987)
[6] K. Riedel et al., NF 28, 1503 (1988)
[7] J.P. Christiansen et al., NF 28, 817 (1988)

Fig. 1

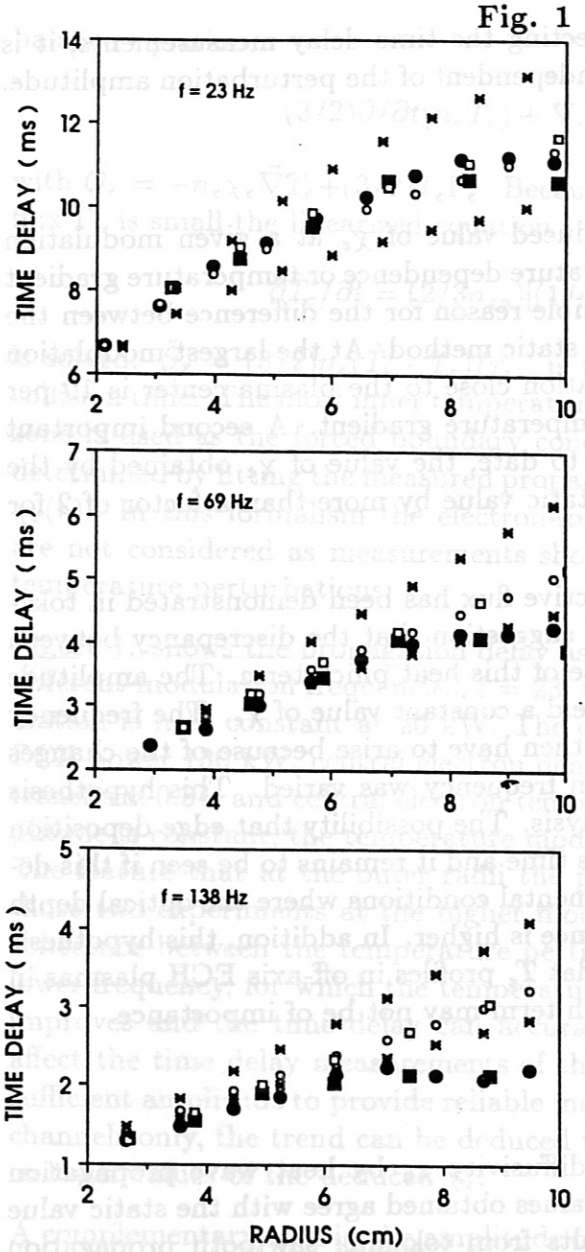

Fig. 2

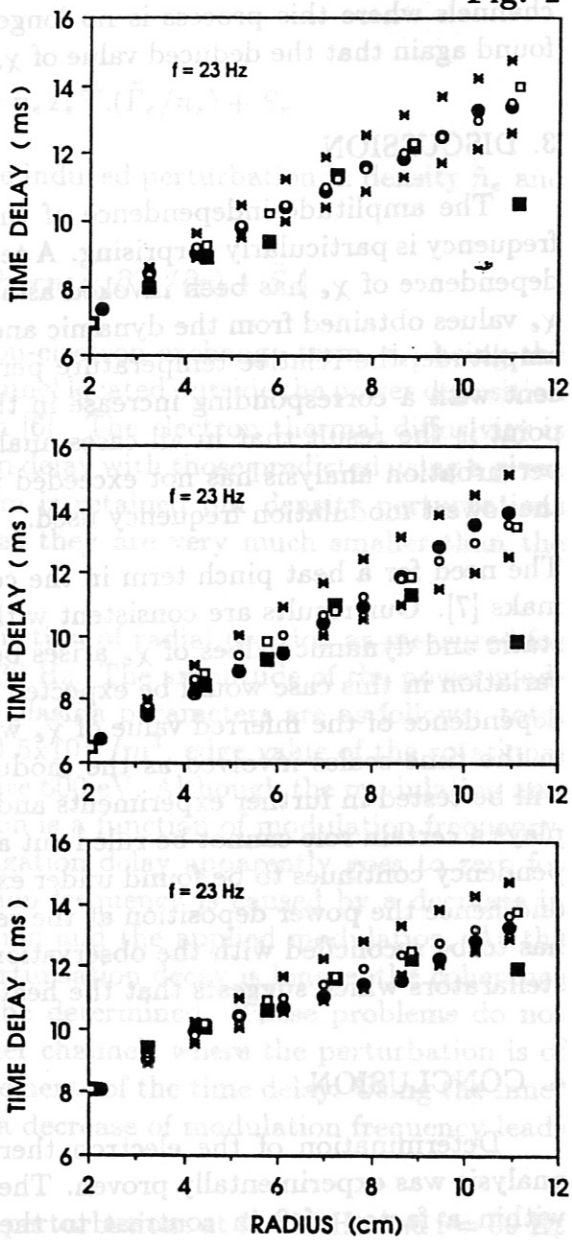

Fig.1 The time delay of the temperature perturbation relative to the modulated power for 3 modulation frequencies is shown. Plotted are the experimental points from measurements on the inside and outside of the plasma column (dark points) and the predicted values of the time delay for $\chi_e = 2\chi_e^{PB}$ (hollow points, PB = stationary power balance). The predicted values of the time delay with $\chi_e = \chi_e^{PB}$ and $\chi_e = 3\chi_e^{PB}$ (crosses) are also shown. The innermost channels show a frequency dependence of χ_e.
Fig.2 The time delay for three different modulation amplitudes is shown. While the relative amplitude in the lower picture is the same as that in the frequency scan, it is increased in the middle and upper picture by a factor of 2 and 4 respectively. The predicted values of the time delay for $\chi_e = 1.5\chi_e^{PB}$ (hollow points) with $\chi_e = \chi_e^{PB}$ and $\chi_e = 2\chi_e^{PB}$ (crosses) are shown. The deduced χ_e values show only a slight variation with modulation amplitude.

IMPURITY BEHAVIOUR IN W7-AS PLASMAS UNDER DIFFERENT WALL CONDITIONS

R. Brakel, R. Burhenn, A. Elsner, P. Grigull, H. Hacker, K. Kondo[+], F. Sardei, U. Schneider, A. Weller, H. Wolff[++], R. Behrisch, D. Hildebrandt[++], H. Renner, J. Roth, E. Taglauer, W7-AS Team, ECRH Group[*], NI Group

Max-Planck-Institut für Plasmaphysik, EURATOM Ass., Garching bei München, FRG

[*] *Institut für Plasmaforschung, Universität Stuttgart, FRG*

[+] *Plasma Phys. Lab., Kyoto University, Japan*

[++] *Zentralinstitut für Elektronenphysik, Berlin, FRG*

Introduction - In the WENDELSTEIN W7-AS stellarator (R = 2 m, a = 18 cm) oxygen, carbon, titanium, and iron appear as dominant plasma impurities originating from the stainless steel wall and the TiC-coated graphite limiters and shieldings. For metallic walls the oxygen flux was minimized by He-glow-discharges and long pulse operation (up to 1.5s). ECRH heated plasmas are only severely affected by impurity radiation at low input power. However, when using NBI heating, impurities play an important role in particular because much higher plasma densities at correspondingly low temperatures are achieved and radiative collapse may occur. Efforts have been made to reduce the impurity radiation by wall conditioning techniques (carbonization and boronization of the inner walls of the vacuum vessel).

Wall conditioning process - In the case of carbonization a thin carbon film of nearly 1000Å thickness was deposited onto the plasma-facing surfaces during glow discharges in 70% He and 30% CH_4 or CD_4. The boronization[1,2] runs were performed in glow discharges with 10% B_2H_6 (diborane) + 90% He at room temperature vessel walls at a typical pressure of 10^{-2} mbar. The operation conditions for the three electrodes toroidally displaced by about 120^o from each other are $\simeq$ 3A and $\simeq$ 600V. An oscillator crystal mounted onto a removable probe allows an on-line determination of the growth of the layer which reached a thickness of 300-800Å. The surface analysis of the probe yielded a mixture of about 60% boron, 30% hydrogen and 10% carbon.

Diagnostic tools - The impurity behaviour was investigated by the SPRED survey spectrometer, a grating- and a crystal-spectrometer in the VUV and X-ray region, soft-X cameras and a bolometer system, respectively. Integral information on impurity fluxes was derived from deposition probe analysis. T_e- and n_e-profile informations at the plasma edge were obtained by Thomson scattering and Langmuir probes.

Carbonization - As compared to experiments with unconditioned walls discharges in the *freshly* carbonized machine show a clear reduction of all impurity species, especially of Ti and Fe. However, O- and C-fluxes could generally be retained only for a few shots and increased to their former level within typically 30 shots. Due to the correlated evolution of O- and C-fluxes CO desorption[3] is probably the predominant release mechanism. The behaviour of Ti released from the TiC-coated limiters strongly depends on the discharge conditions (T_e, n_e, heating power). For high density, low temperature ECRH as well as NBI heated discharges Ti-fluxes are persistently suppressed by carbonization. However, running low density, high temperature ECRH-discharges directly after carbonization causes Ti-radiation to raise rapidly to its pre-carbonization value due to erosion of the carbon layer on the limiters. Fe-radiation remains

efficiently reduced indicating a long persistance of the carbon layer on the less loaded metallic walls. Density control was not possible after carbonization because of a recycling coefficient $\gtrsim 1$. Repeated application of Helium glow discharge conditioning improved the recycling behaviour and transiently reduced O- and C-fluxes by a factor of up to 10.

Boronization - In a second step W7-AS was boronized after removal of the carbon layer. In contrast to carbonization the boron coating leads to a remarkable and durable retention of oxygen and - because CO desorption is thereby largely reduced - consequently of carbon (fig.1a). After a short-term reduction by a factor of $\simeq$ 50–100 directly following a new boronization the spectroscopically measured C- and O-fluxes approach stationary values of only 0.1–0.2 as compared to the unconditioned case. Ti is only transiently reduced and even raises by a factor of $\simeq 2$ above its pre-boronization value (fig.1b). This indicates that the boron layer is eroded from the limiters within a few shots, which is also evident from the fast increase of CIII-emission in the transient phase. This is generally observed for the various operating conditions. The final level observed for Fe was by a factor of $\simeq 2$ lower than before boronization.
In addition Ti- and Fe-fluxes within the SOL were analyzed by radially resolving deposition probes (fig.1c). Γ_{Ti}/Γ_{Fe} was about 2 for an ECRH reference discharge before boronization. After boronization (and erosion of the boron coating from the limiters) Γ_{Ti} was increased by a factor 2.5 wheras Γ_{Fe} was decreased by the same factor. These values are consistent with the spectroscopic results. The effect of boronization on impurities is also demonstrated by the central soft-X line radiation (fig.2) measured in comparable ECRH-heated discharges under steady state wall conditions.
The increased Ti level is explained by generally higher edge temperatures after boronization due to reduced low-Z radiation losses in the plasma edge region. Consequently

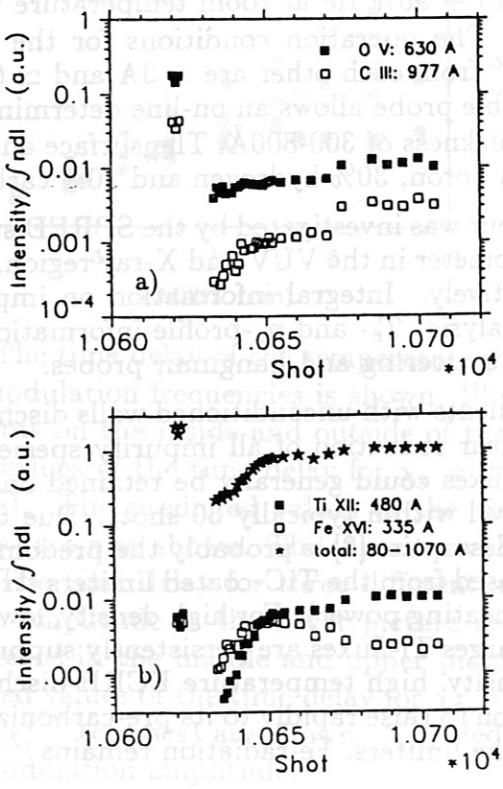

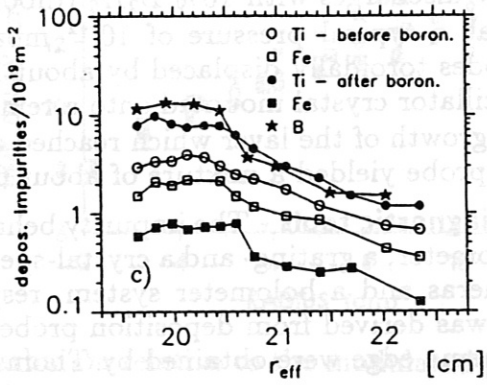

Fig.1: Effect of boronization on impurities in ECF-heated W7-AS plasmas.
Pulse-to-pulse evolution of impurity radiation in response to boronization after pulse #10624 (1a and b, from SPRED).
Deposited impurities as functions of the effective radius (the limiter position is 18cm). The probe was exposed to 10 ECRH reference discharges before and after boronization (1c).

the limiter loads are significantly enhanced (up to a factor of 2.5 as measured by limiter calorimetry) which causes erosion of the boron coating and Ti as well as C release from the limiters. This conclusion is supported by T_e- and n_e-profiles from Thomson scattering in the plasma edge region and from Langmuir probes in the SOL (fig.3). The ion flux across the last closed magnetic surface was approximately constant before and after boronization in this case. A significant increase of the edge temperature was also observed for discharges with the central density kept constant.
In spite of the quick erosion of the boron layer from the limiter there remains a long lasting beneficial effect on the reduction of low-Z materials and of iron as well as on the recycling behaviour probably due to a still existing layer on the vessel wall.
Immediately after boronization the accessible parameter range for ECRH and NBI heated plasmas was substantially extended. Low power (< 200kW) ECRH-operation near the cut-off density was possible and a significant increase of the energy replacement time up to 40ms was achieved. With boronized walls discharges at stationary densities with constant gas-flux could be obtained (recycling coefficient $\lesssim 1$). In NBI-heated discharges (absorbed power = 1.1MW) record values in energy content of up to 33kJ ($\langle\beta\rangle$=0.7% at 2.5T) at an averaged density of $3{\cdot}10^{-20}m^{-3}$ were observed.

Radiation Calculations - The radiated power measured by the soft-X cameras and the bolometer system has been modelled by the IONEQ radiation code with measured T_e- and n_e-profiles as well as spectroscopic line informations (O, C, Fe) as input data. The Ti-concentrations were derived from simulation of He- and H-like radiation as observed in the PHA-spectra taking into account also contributions of satellite lines (the values from this analysis are believed to be reliable within a factor of $\simeq 2$).
With unconditioned (decarbonized) vessel an impurity composition of approximately 6% C, 3% O, 0.3% Ti and 0.02% Fe ($Z_{eff} \simeq 5$) was estimated for ECRH-discharges (P_{ECRH}= 340kW, n_e=$3{\cdot}10^{13}cm^{-3}$) compared to roughly 1% C, 0.6% O, 0.6% Ti and 0.01% Fe ($Z_{eff} \simeq 4$) in the boronized machine. The main contributors to Z_{eff} in the unconditioned case are O and C wheras Ti becomes important after boronization. For high density NBI-discharges Z_{eff} is below 1.5.

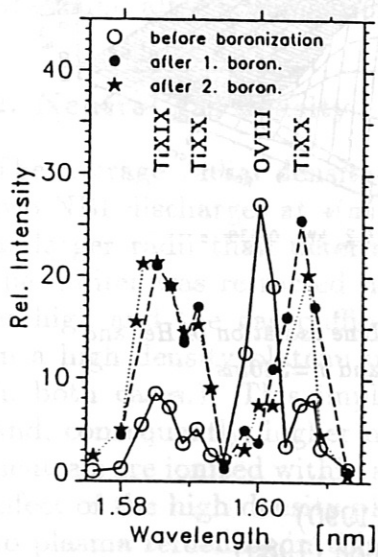

Fig.2: Soft-X ray spectra from ECF-heated W7-AS plasmas before and after boronization.

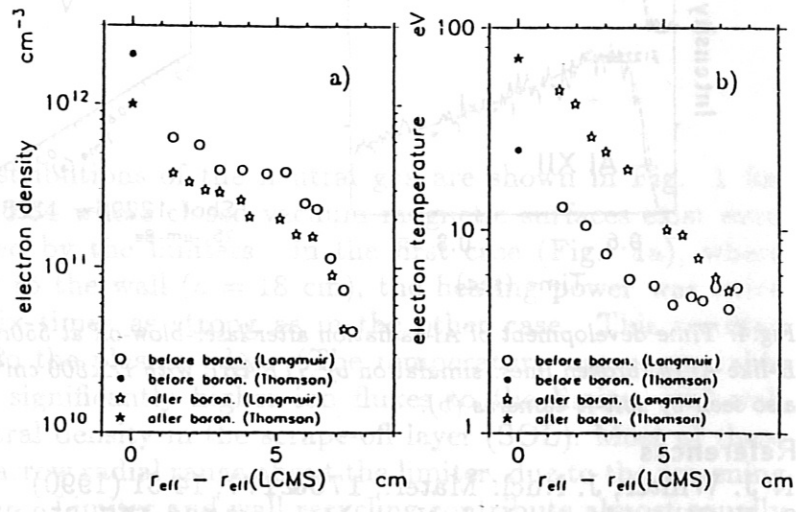

Fig.3: Radial decay of SOL density (a) and temperature (b) for ECRH reference discharges before (#10608–10619, $\bar{n}_l$= $1.4{\cdot}10^{19}m^{-3}$) and after (#10674–10685, $\bar{n}_l$=$1.1{\cdot}10^{19}m^{-3}$) boronization (from Langmuir probe and Thomson scattering). P_{ECRH}=180kW, B=2.5T, ι_a=0.34.

Impurity transport studies - The impurity transport has been investigated by Laser blow-off technique with aluminium as tracer impurity. The diffusion coefficient D (taken constant over radius with radially increasing convection velocity) and the particle confinement time τ for Al were obtained from fitting the temporal decay of the density of the injected tracer impurity represented by the Al-radiation with the STRAHL[4] transport code.
ECRH-heated discharges at 2.5T in the unconditioned vacuum vessel show a significant increase (by a factor of $\simeq 4$) of the impurity confinement time to 40-70 ms and a similar decrease of the diffusion coefficient to 1000-2000 cm^2/s as compared to experiments at half the toroidal magnetic field (1.25T) and lower electron density. Convection is not important: Omitting the convective velocity in the transport calculations leads to a reduction of only 20 % for D. Additionally a clear dependence of the confinement time on the plasma aperture (approximately $\propto a^2$) was observed while D remained nearly unchanged. Normalization by this scaling strongly reduces the scattering of the experimental values obtained also from other discharges. Measurement of the confinement properties at different ECRH input powers or rotational transforms show no clear dependence within the error bars. After boronization the machine could also be operated under discharge conditions (high density n_e=3.8- 4.7·$10^{13} cm^{-3}$, full aperture a=18cm) leading to aluminium confinement times of up to nearly 340ms for ECRH-input powers of 170 and 350kW at ι=1/3 (fig.4) and even significantly larger at ι=1/2. A strong dependence of τ on plasma radius and electron density is noted. Diffusion coefficients of 500-1100 cm^2/s were derived wheras a moderate inward velocity was now required to simulate the discharges with long confinement times. The latter concerns also the analysis of a stationary NBI-heated discharge (440 kW) where $D \simeq 700\ cm^2/s$ and $\tau \simeq 400$ ms were observed.

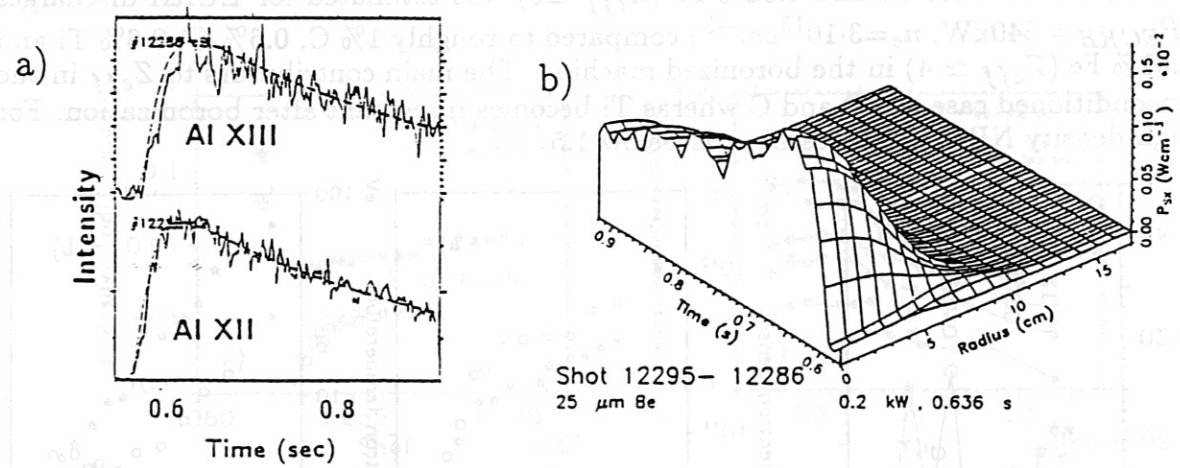

Fig.4: Time development of Al-radiation after laser-blow-off at 550ms: Line radiation of He- and H-like Al (a, broken lines: simulation by STRAHL with D≃800 cm^2/s and τ=340ms) also seen by soft-X cameras (b).

References

1. J. Winter, J. Nucl. Mater., **176&177**, 14-31 (1990)
2. U. Schneider et al., J. Nucl. Mater., **176&177**, 350-356 (1990)
3. V. Philips et al., Plasma Phys. and Contr. Fusion, **31**, 1685 (1989)
4. K. Behringer, JET-R (87)08 (1987)

PARTICLE TRANSPORT AND PLASMA EDGE BEHAVIOUR IN THE W7-AS STELLARATOR

F. Sardei, H. Ringler, P. Grigull, A. Dodhy, G. Kühner, H. Maassberg,
F.P. Penningsfeld, W7-AS Team, NBI Team
Max-Planck-Institut für Plasmaphysik, IPP-EURATOM Ass.,
D-8046 Garching, Germany

ECRH Group
Institut für Plasmaforschung der Universität Stuttgart
D-7000 Stuttgart, Germany

1. Introduction

The particle transport in W7-AS is investigated by coupling DEGAS code /1/ simulations with H_α emissions measured at different toroidal positions. Radially resolved ion fluxes are obtained from the calculated ion source distributions, after calibrating the recycling fluxes with the H_α signals /2/. Additionally, for NBI discharges, radial profiles of the neutral beam halo and of the beam deposition are taken from FAFNER code /3/ calculations. Several NBI discharges at 2.5 T, with 350 and 700 kW heating power and different plasma densities and limiter apertures, have been analyzed and compared with ECRH discharges.

Wall conditioning by carbonization or boronization has turned out to be very beneficial for reducing the radiation losses in W7-AS. Along with a clear reduction of the impurity radiation losses, both the edge electron temperature and the measured limiter thermal load increased after boronization for otherwise unchanged external machine operation parameters. On the other hand, no change of the local particle transport properties was found after boronization.

2. Neutral gas density

The average radial density distributions of the neutral gas are shown in Fig. 1 for two NBI discharges at $\iota(a) = 0.34$ where closed vacuum magnetic surfaces exist even at larger radii than determined by the limiters. In the first case (Fig. 1a), where the limiter was retracted near to the wall ($a = 18$ cm), the heating power was twice as high and the gas puffing six times as strong as in the other case. This resulted in a high density plateau up to the plasma edge. (The temperature was comparable in both cases.) This implies significantly higher ion fluxes to the limiter and wall and, consequently, higher neutral density in the scrape-off layer (SOL). Most of these neutrals are ionized within a narrow radial range about the limiter, due to the screening effect of the high density plasma. Limiter and wall recycling contribute almost equally to plasma refuelling in this case. In the small limiter aperture case ($a = 12$ cm), the limiter recycling is dominant. The beam halo is generally negligible in the outer plasma region and dominant in the center, except for low density, small size plasmas, for which central refuelling by limiter recycling is not negligible, as shown in Fig. 1b. Neutrals

from recombination are ignored, as they are negligible fractions of the total densities both in the bulk and edge plasma regions.

Concerning the effect of the neutrals on the ion power balance in W7-AS, charge exchange with the thermal ions, which is calculated by DEGAS code, is shown to be relevant only for low density ECRH discharges /4/. Charge exchange with the fast NBI ions can be neglected in W7-AS as long as the neutral gas density does not exceed the order of $10^{10} cm^{-3}$ in the plasma edge and decays radially at least two orders of magnitude to the plasma center. Finally, charge exchange with the impurities leads to a shift of the ionization equilibrium to lower ionization states. This effect is generally weakened by strong impurity transport. Still it may result in an enhancement of the total radiation losses by more than a factor of two, if low Z impurities are dominant.

3. Particle transport

In order to obtain particle fluxes and diffusion coefficients, the beam deposition and the halo effects have been included in the evaluation of the particle balance. The beam deposition is typically distributed over a radial range of more than 10 cm. It represents the main plasma refuelling in the plasma center, and hence it provides the central particle flux. However, the global plasma density level is sustained to more than 90 % by particle replacement from recycling processes, which play the dominant role in the density gradient region and in the plasma edge. (Refuelling rates of $1.5 \cdot 10^{20} s^{-1}$ from 700 kW NBI input power compares, for example, to limiter and wall recycling rates between 30 and 100 times larger, depending on plasma density and limiter position.) The halo effects do not play a major role in the plasma particle balance, since the radial distribution of the ionizing halo neutrals inside the bulk plasma is very similar to that of the ion sink where the halo neutrals originate.

A comparison of the ion fluxes, as simulated by DEGAS code, with neoclassical predictions with and without ambipolar electric field (ion root, $E_r < 0$) /4/ is shown in Fig. 2 for two ECRH and NBI discharges, heated by 140 and 700 kW, respectively. In both cases the neoclassical ion fluxes without electric field are more than one order of magnitude larger than the ambipolar fluxes. In the bulk part of the plasma the simulated fluxes (thick broken lines in Fig. 2) agree reasonably well with neoclassical predictions (dot-dashed lines). At outer radii the particle losses are enhanced and strongly increase with radius, whereas the neoclassical losses typically decrease. From several analyzed ECRH and NBI discharges there is a clear indication that the gap between the two fluxes in the outer confinement region increases with decreasing density. A similar radial behaviour is found by comparing the diffusion coefficients, as derived from the usual diffusive ansatz for given fluxes and density gradients, with neoclassical calculations /5/.

Diffusion coefficients $D_{\perp a}$ at the last closed magnetic surface (LCMS) derived from DEGAS code calculation and Langmuir probe data are compared in Fig.3 as a function of the LCMS plasma density n_{ea}. Included are ECRH and NBI heated discharge with $\iota_a \approx 0.34$ and minimum or maximum limiter apertures ($a = 12$ or 18 cm, respectively, for simplicity not labelled in the figure). LCMS electron temperatures were between 40 and 120 eV. Values from probe data were estimated by the

relation $\lambda_n = (D_{\perp a} 2L_C/c_s)^{1/2}$ (λ_n = SOL density decay length, connection length $2L_C \approx m2\pi(R^2 + \iota^2 a^2)^{1/2}$) except for discharges with small limiter apertures, where significant SOL recycling occurred (about 50%, from DEGAS modelling). In these cases an analytical correction was applied /6/, which takes into account n_e profile broadening in the SOL. Furthermore $T_e = T_i$ was generally assumed within the SOL.

In contrast to higher rotational transforms ($\geq 1/2$), where the boundary magnetic field topology is characterized by a separatrix and by significant poloidal and toroidal inhomogeneities due to $5/m$ resonances ($\iota = n/m$) /7/, this low-ι configuration has "smooth" magnetic surfaces within the SOL. The diffusion coefficients shown in Fig.3 indicate a $D_{\perp a} \sim n_{ea}^{-1/2}$ scaling, which seems to be independent of the heating scheme and limiter aperture. The $D_{\perp a}$ values are by factors about 2 - 5 below the Bohm values. A temperature dependence of $D_{\perp a}$ cannot be resolved from these data.

References

/1/ V.V. Afrosimov et al. (1980), Sov. J. Plasma Phys., **6**, 133
/2/ F. Sardei et al. (1990), ECA, 17th EPS Conf. on Contr. Nucl. Fus. and Plasma Physics, Amsterdam 2, 471
/3/ G.G. Lister et al. (1983), **ECA 7D-II** (11th EPS, Aachen), 323
/4/ V.I. Afanasiev et al. (1991), this Conference
/5/ H. Ringler et al. (1990), Plasma Phys. and Contr. Fus., **32**, 933
/6/ P.C. Stangeby and G.M. McCracken (1990), J. Nucl. Fusion, **30**, 7, 1225
/7/ P. Grigull et al. (1990), J. Nucl. Materials **176 & 177**, 975

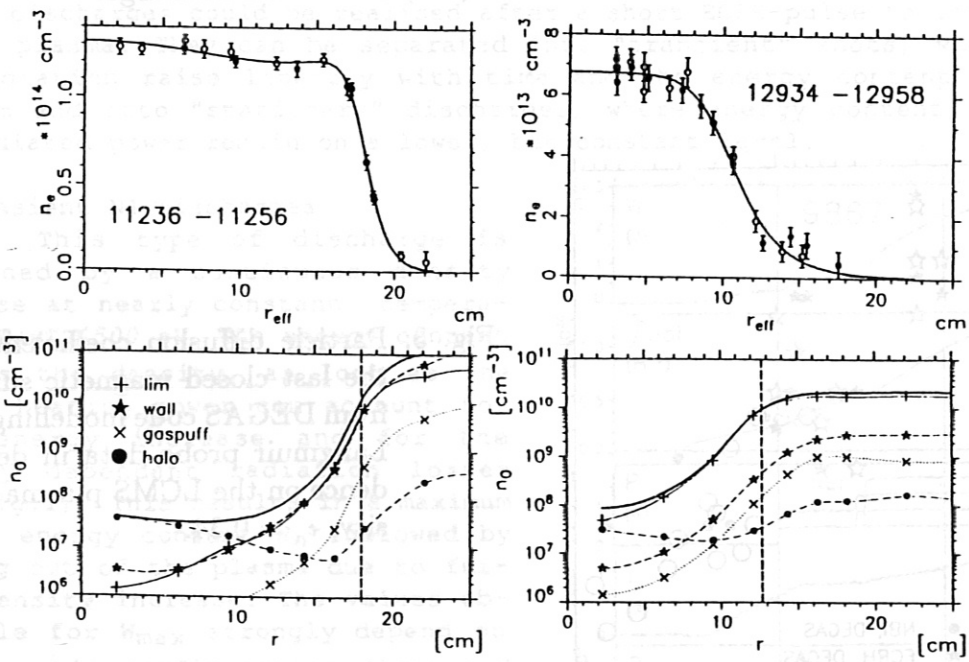

Fig. 1: Electron and neutral density profiles for two NBI heated discharges at $\iota_a = 0.34$ with large ($a = 18\ cm$, Fig. 1a) and small ($a = 12\ cm$, Fig.1b) limiter apertures.

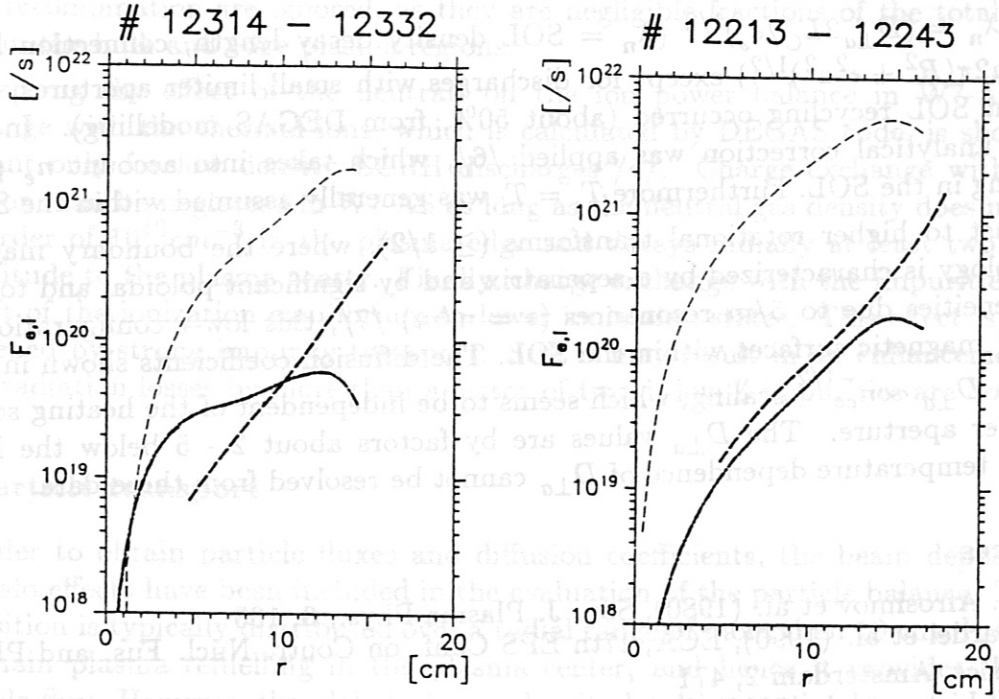

Fig. 2: Comparison of ion fluxes from DEGAS code simulation (thick broken lines) and neoclassical predictions with (dot dashed lines) and without (thin broken lines) ambipolar electric field for an ECRH (left) and a NBI discharge.

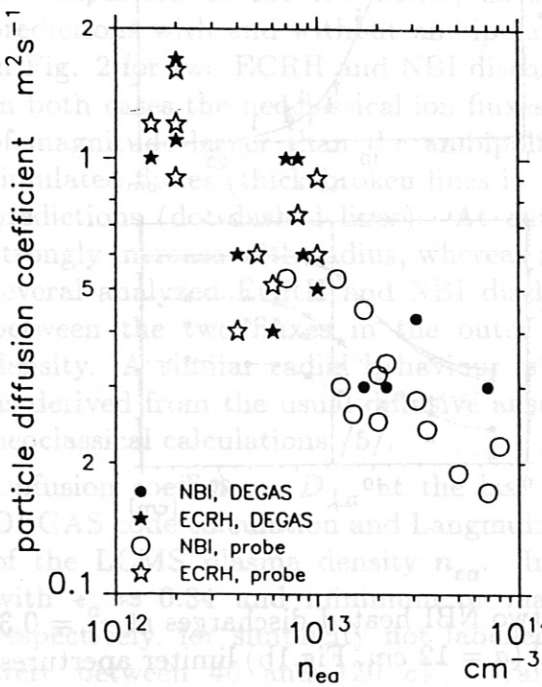

Fig. 3: Particle diffusion coefficients at the last closed magnetic surface from DEGAS code modelling and Langmuir probe data in dependence on the LCMS plasma density, $\iota_a = 0.34$.

NEUTRAL INJECTION EXPERIMENTS ON W7AS STELLARATOR

F.-P. Penningsfeld, W. Ott, W7AS Team,
ECRH Group, NI Group, Pellet Injection Group

Max-Planck-Institut für Plasmaphysik, Euratom Association
D-8046 Garching bei München

The neutral beam system of the stellarator W7AS [1] (R_o = 200 cm; a = 20 cm) consists of two ASDEX-type injector boxes installed in opposite direction to allow for balanced NI as well as for co and counter current drive [2]. At present only two of the four source positions on each beam line are equipped with sources labelled "inner" and "outer". The absorption path length of the "inner" sources is about 2.5 m with tangentially penetration, whereas the "outer" sources inject at a steeper angle with an absorption length of 0.7 m. The total neutral power delivered to the torus is 1.6 MW produced by hydrogen beams of 4 sources (45 kV / 24 A). The neutral power species mix is 36:32:32.

During the experimental period in 1990 the wall conditions of W7AS were changed by carbonisation and boronisation of the vessel starting from the pure stainless steel wall. Under all conditions, purely neutral beam heated discharges could be realised after a short ECRH-pulse to initiate a target plasma. They can be separated into "transient" shots, where ∫ndl and radiation raise linearly with time and the energy content shows a maximum and into "stationary" discharges, where energy content, density and radiated power remain on a lower, but constant level.

I) Transient NI-discharges

This type of discharge is gouverned by a continuous density increase at nearly constant temperatures $T_i \approx T_e \leq 500$ eV. The energy content follows the density, as long as the actual heating power can account for this energy increase and for the density dependent radiation losses (see Fig.1). This results in a maximum of the energy content W, followed by cooling out of the plasma due to further density increase. The values obtainable for W_{max} strongly depend on the magnetic configuration (iota and shear [3]) but also on the wall conditions. I_p depicts the bootstrap current, because balanced injection without inductive current drive was applied. The time development of I_p is dominated by the long L/R time con-

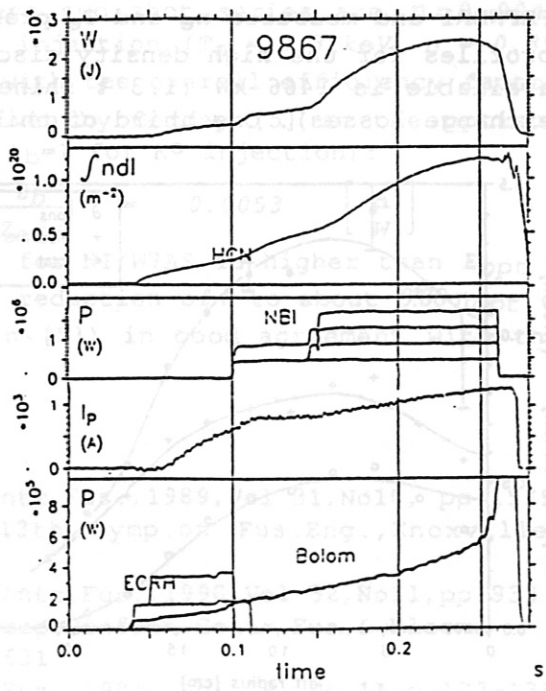

Fig.1: Balanced NI-heated discharge

stant of W7AS. Fig.2 shows the total energy W versus line density for NI-discharges. W increases proportional to $\overline{n}_e$ and is independent of the wall conditions. T_e and T_i may be restricted to constant values due to power dependent neutral particle fluxes and recycling. Using the inner sources only, a similar behaviour is observed. Fig.3 compares a number of NI-discharges at $B = 2.5\ T$ under different wall conditions. W_{max} increases linearly with $\overline{n}_e$, but only after wall conditioning the access to $\overline{n}_e \approx 3x10^{20}\ m^{-3}$ became possible. This corresponds to $\overline{\beta} \approx 0.7$ % and $\beta(o) \approx 1.5$ %.

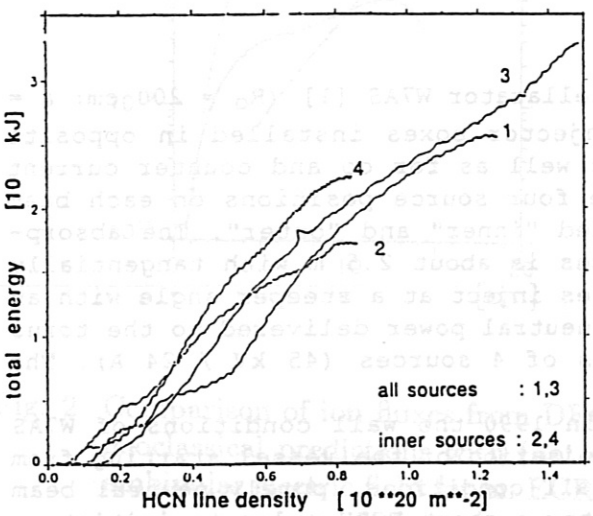

Fig.2: Total energy versus line density; carbonised 1,2 ; boronised: 3,4

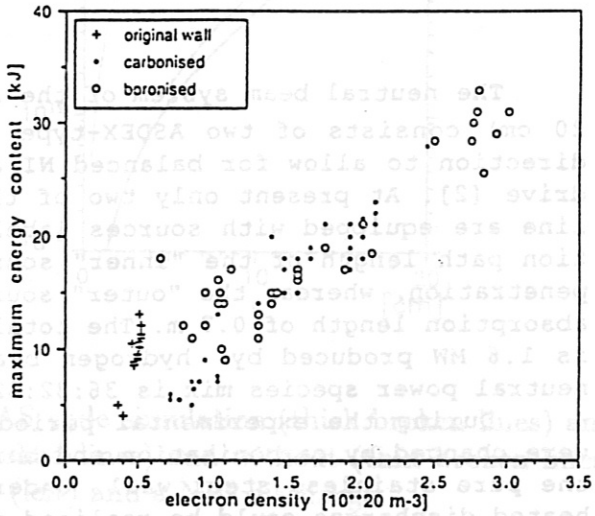

Fig.3: maximum energy versus $\overline{n}_e$ for $350 < P_{ni} < 1500$ kW

The actual NI heating power is calculated using the Monte Carlo code FAFNER1 and measured n_e and T_e profiles. Fig.4 shows the resulting heating profiles for the high density discharge given in Fig.1. The heating power available is 1466 kW (1.3 % shinethrough losses, 8.0 % orbit and charge exchange losses). One third of this power couples directly to the ions and

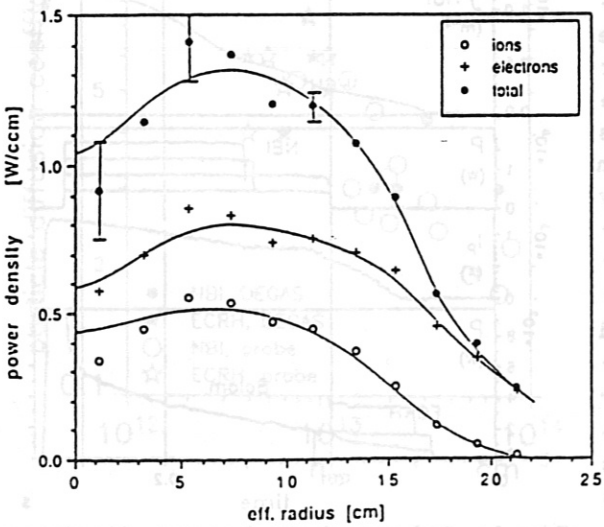

Fig.4: NI heating profile for shot 9867 as calculated with FAFNER1

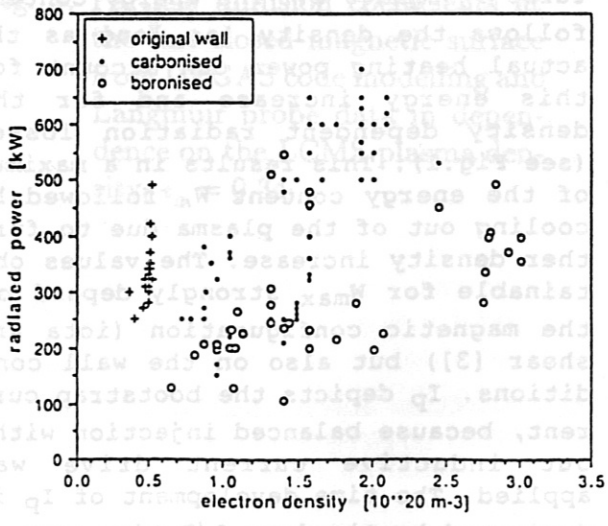

Fig.5: Radiated power at $\dot{W} = 0$ versus averaged density

Fig.7a,b show the result for co and counter injection. In both cases one starts with balanced injection and switches off one source. No ohmic current is induced, so that the measured current Ip is the sum of bootstrap current $I_{boot}(t)$ and $I_{NB}(t)$. By definition 'CO' injection means, that I_{NB} increases the rotational transform as the bootstrap current does in W7AS. The residual current $I_{res}(t) = I_p(t) - I_{NB}(t)$ agrees fairly well with I_{boot} calculated at the time where the density and temperature profiles were measured if $Z_{eff} \approx 2$ is assumed (fat black points).

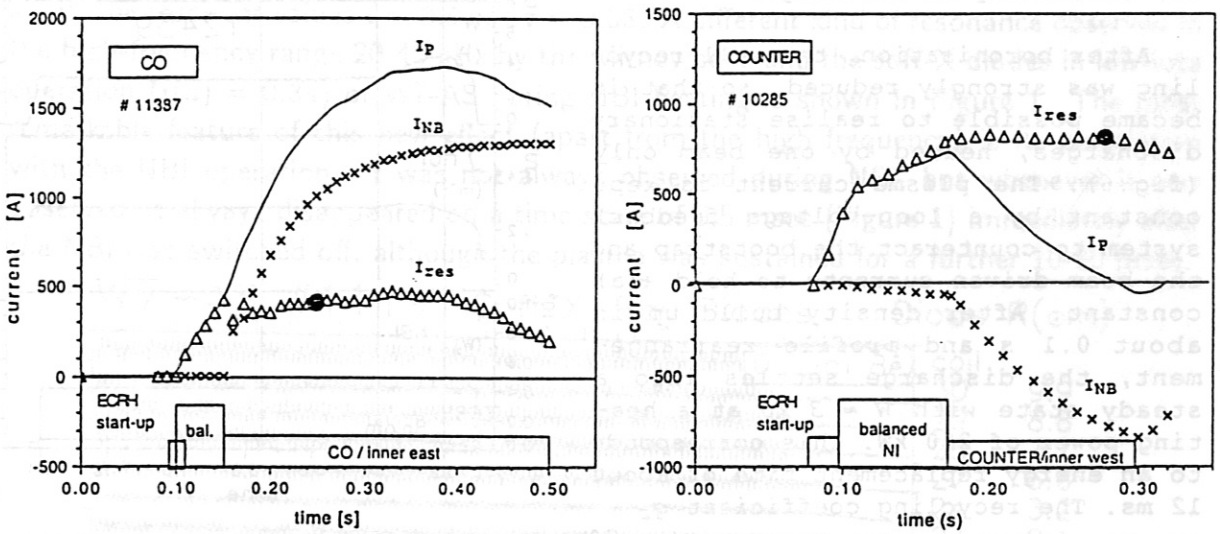

Fig.7a,b: comparison of the calculated beam driven current $I_{NB}(t)$ with the measured plasma current Ip(t) for CO(a) and COUNTER(b) injection.

The current drive efficiencies for these two shot series are $\eta = 0.0040$ *A/W* for CO resp. *0.0031 A/W* for COUNTER injection ($T_e \approx 0.3$ *keV*, $n \approx 0.85$ $[10^{20} m^{-3}]$). These results compare well with the overall efficiency factor η for current drive by fast ions as given by Cordey [5] at the optimum injection energy $E_{opt} = 40\, A_b\, T_e$ (Z_b=1, A_b=1 for H° injection):

$$\eta_{opt} = \frac{I}{P} \cong \frac{0.06\ \bar{T}_e}{\bar{n}\ R_o\ Z_b} \left(1 - \frac{Z_b}{Z_{eff}}\right) = 0.0053 \left[\frac{A}{W}\right]$$

The averaged injection energy of 30 keV for NI/W7AS is higher than E_{opt} = *12 keV* for T_e = *0.3 keV* and therefore a reduction of η to about $0.80\,\eta_{opt}$ = *0.0042* has to be expected (see Fig.2 in [5]) in good agreement with the experimental results.

References

[1] H.Renner et al., Plasma Phys.& Contr.Fus.,1989,Vol 31,No10, pp 1579

[2] F.-P.Penningsfeld et al.,Proc.13th Symp.on Fus.Eng.,Knoxville, 1989, Vol I,p 288-29

[3] H.Ringler et al., Plasma Phys.& Contr.Fus.,1990,Vol 32,No11,pp 933

[4] U. Gasparino et al., Proc.16th Europ.Conf.on Contr.Fus.& Plasma Phys.,Venice(IT),1989,Vol II, pp 631

[5] J.G.Cordey, Plasma Phys. & Contr.Fus.,1984, Vol 26, No 1A,p 123-132

two thirds to the electrons. This is due to the low electron temperature, which reduces the critical energy to about 7 keV. The radiated power at $dW/dt = 0$ depends on the corresponding density, but also on the wall conditions as shown in fig.5. By reducing P_{rad} first by carbonisation and furthermore by boronisation, the operational regime could be extended to higher densities. Some relatively high radiation losses in the boronised case are caused by first operation at $\iota = 0.53$, usually $\iota \approx 0.34$ was used, so that new parts of the vessel came into contact with the plasma edge.

II) Stationary NI-discharges

After boronisation, the wall recycling was strongly reduced, so that it became possible to realise stationary discharges, heated by one beam only (fig.6). The plasma current is kept constant by a loop-voltage feedback system to counteract the bootstrap and the beam driven currents to hold $\iota(a)$ constant. After density build up in about 0.1 s and profile rearrangement, the discharge settles into a steady state with $W \approx 3$ kJ at a heating power of 250 kW. This corresponds to an energy replacement time of about 12 ms. The recycling coefficient q_r can be estimated using $\bar{n} = 0.35 \times 10^{20}$ m^{-3}, $V_p = 1.14\ m^3$ and the actual beam fueling rate $S_{ni} = 0.58 \times 10^{20}\ s^{-1}$ (one inner source with about 30% shinethrough at this density):

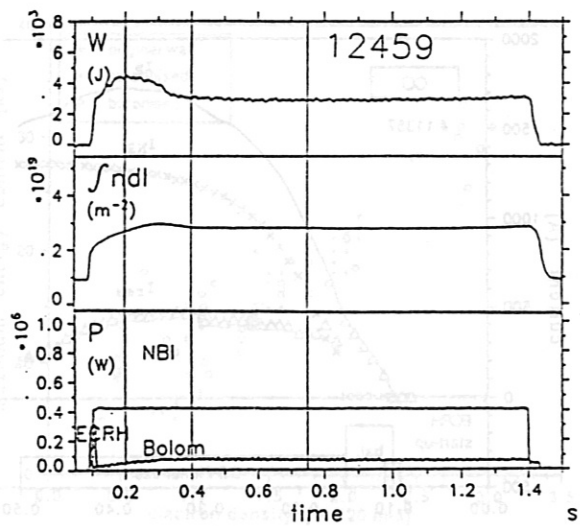

Fig.6: Stationary NI-discharge

$$\dot{n} = 0 = \frac{\bar{n}}{\tau_p}\left(q_r - 1\right) + \frac{S_{ni}}{V_p}$$

For stationarity reasons $q_r < 1$ is necessary and assuming a global particle confinement time τ_p of about 0.1 s $q_r \approx 0.85$ is obtained.

III) Neutral beam current drive

From the known birth profile of injected ions as given by FAFNER1, the radially resolved distribution function $f_i(\vec{v}, r)$ of fast ions can be calculated, if it is assumed that the ions slow down within the radial layer they were born. By integration of $f_i(\vec{v}, r)$ over the velocity space the fast ion current density $j_{fi}(r)$ is obtained. The beam-driven current density $j_{bd}(r)$ then can be calculated using the trapped electron fraction f_t[4]:

$$j_{bd}(r) = j_{fi}(r)\left(1 - \frac{Z_b}{Z_{eff}} f_c(r)\right) \quad ; \quad f_c = 1 - f_t$$

The observable beam-driven current $I_{NB,max}$ is the integral of j_{bd} over the plasma cross section. After beginning of the injection at $t = t_o$ this driven current develops with a time constant $\tau = L/R$ (about 0.1 s for W7AS discharges) and therefore the time dependence can be represented by:

$$I_{NB} = I_{NB,max}\left(1 - e^{-\frac{t - t_0}{\tau}}\right)$$

EPS Conference, 3-7 June, Berlin FRG

MHD Activity Driven by NBI in the W7-AS Stellarator

A. LAZAROS, R. JAENICKE, A. WELLER
MAX-PLANCK-INSTITUT für Plasmaphysik, IPP-EURATOM Association
8046 Garching bei München, F. R. GERMANY

1. Introduction

The $m = 2, n = 1$; $m = 3, n = 1$ resonant modes have been previously observed [1] in the low-frequency band of 1-5 kHz by the soft-X diodes in W7-AS during iota scans about the resonant values $i = 0.5$ and $i = 0.33$. A different kind of resonance observed in the high-frequency range 20-40 kHz by the Mirnov coils and the soft-X diodes in low-iota operation ($i(a) = 0.34$) of W7-AS during NBI heating is shown in Figure 1. The most remarkable feature of this new effect (apart from the high frequency) is its correlation with the NBI operation. It was not always observed during NBI, but whenever it was observed, it always disappeared on a time scale of 0.5 msec (Figure 1) immediately after the NBI was switched off, although the plasma was sustained for a further 10-20 msec.

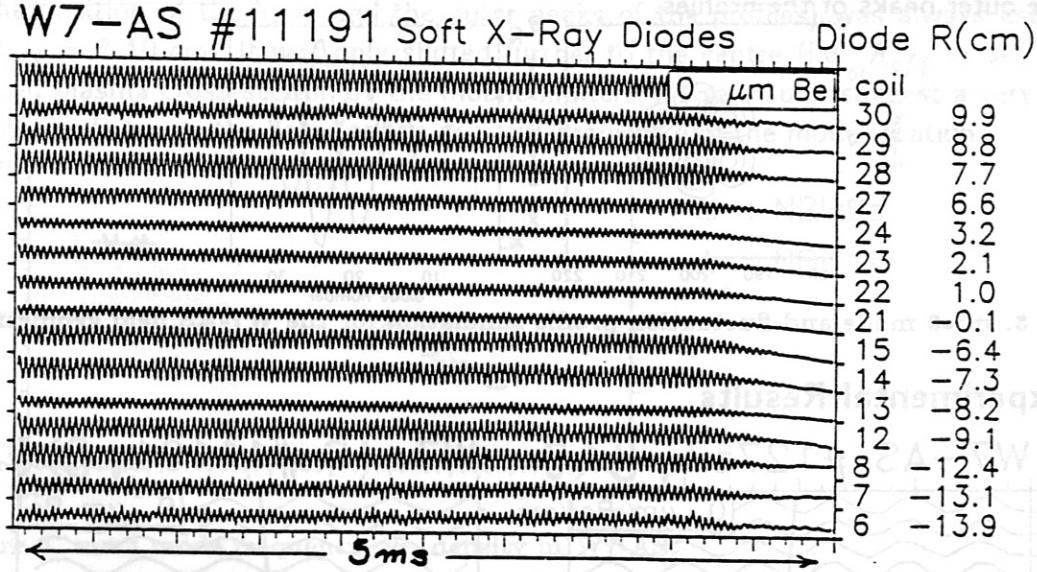

Figure 1. X-ray and magnetic fluctuations before and after NBI termination.

2. Mode Analysis Technique

X-ray fluctuations in W7-AS are investigated by two pinhole cameras (each one of which has 36 diodes) at the same toroidal location. Magnetic fluctuations are measured by two poloidal arrays of Mirnov coils (each one of which has 8 coils) at two different toroidal locations. Mode analysis carried out by both diagnostics provided similar results. They both agree in the poloidal mode number m and the poloidal rotation. In addition to this, the X-ray diagnostics (looking into the plasma) provide the location of the resonant surface and the Mirnov coils provide the toroidal mode number n. Simulated X-ray fluctuations for the $m = 3$ mode, in particular, in a circular plasma (for simplicity) and pinhole camera geometry are shown in Figure 2. The rotation (of any mode) is indicated

by the phase propagation (represented in Figure 2 by the dashed lines), and the $m = 3$ structure is identified from the three phase inversions along the phase propagation.

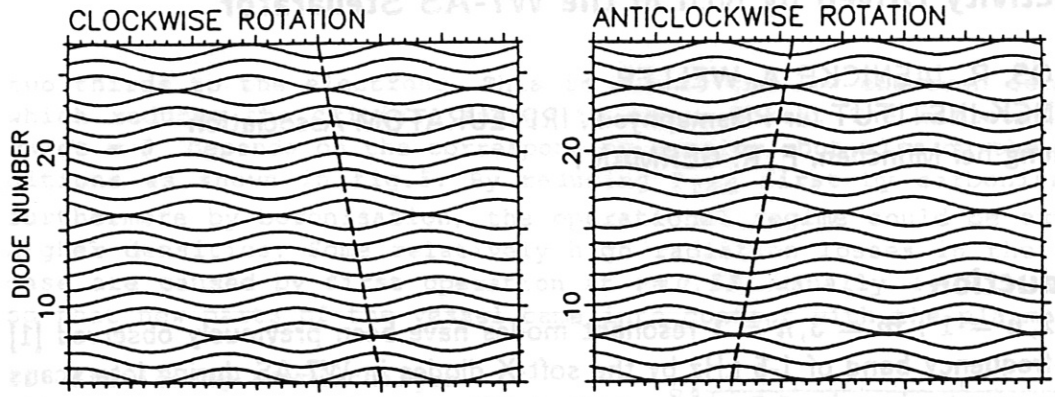

Figure 2. X-ray fluctuations simulation for the rotating m=3 mode.

The $m = 3$ mode configuration and the corresponding X-ray fluctuation profiles (when the mode is at the phase of 0° and 180°) for the precise W7-AS field geometry are shown in Figure 3 (one can see also in these profiles the three phase inversions due to the $m = 3$ structure). The location of the resonant surface is indicated by the position of the inner and the outer peaks of the profiles.

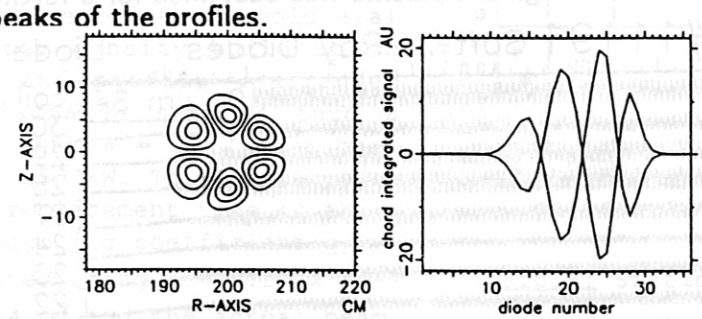

Figure 3. m=3 mode and fluctuation profile simulation for the W7-AS field geometry.

3. Experimental Results

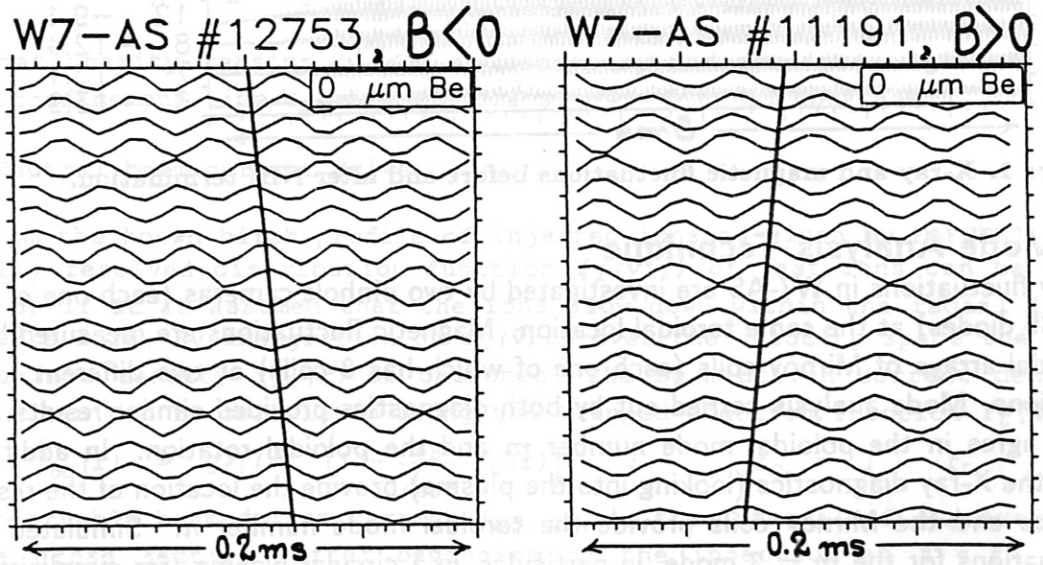

Figure 4. X-ray fluctuations at positive and negative field in W7-AS.

X-ray fluctuations from the intense mode activity of Figure 1 at positive (+2.5T) and negative (-2.5T) field are shown in Figure 4. These raw signals in comparison with the simulated ones of Figure 3 clearly indicate the $m = 3$ mode ($n = 1$ as obtained by the Mirnov coils), which rotates in opposite directions when the field is reversed. The direction of the rotation is identified as the ion diamagnetic drift.

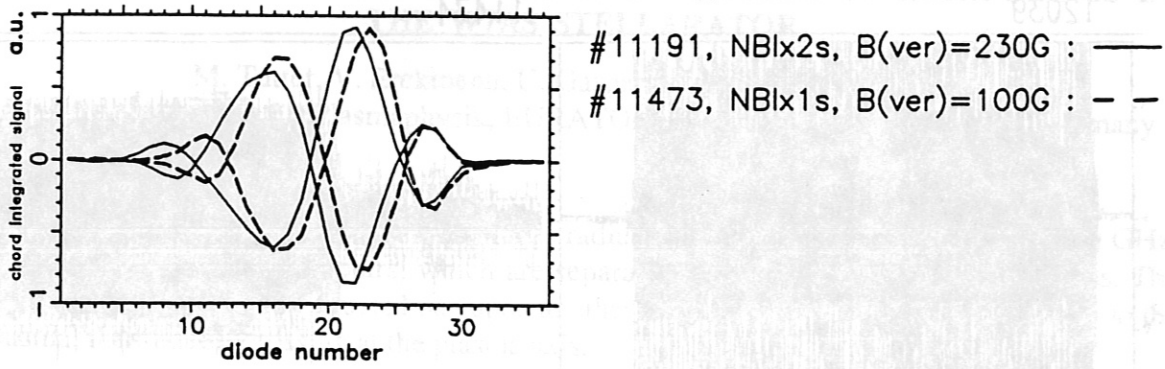

Figure 5. X-ray fluctuation profiles due to the m=3 mode in W7-AS.

Typical and well-reproducible fluctuation profiles are shown in Figure 5. One can see a similar structure (to that of the simulated profiles), apart from a relative displacement to the inside because of the applied positive vertical field. The resonant surface (located by the position of the inner and the outer peaks of the profiles) was always estimated at R_{eff} = 7-10 cm. It was only shifted further to the centre (i.e. R_{eff} = 5-7 cm) at reduced plasma cross-section by the mobile limiter. These results suggest a very strong correlation between the beta (or the density) gradient and the mode location.

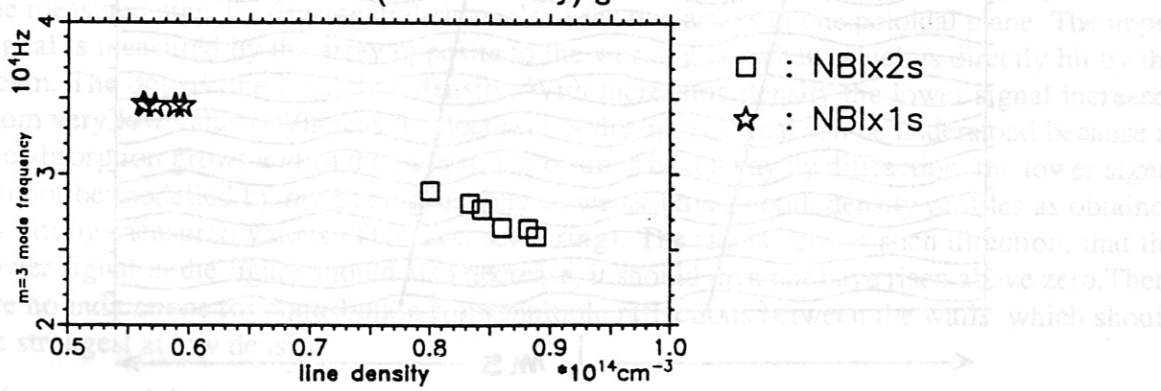

Figure 6. m=3 mode frequency -vs- density in W7-AS.

The mode frequency -vs- density plot (Figure 6) shows an inverse relation in the frequency range 20-40 kHz. It seems that there is a critical line density limit of $10^{14} cm^{-3}$ above which the mode has never been observed. It has been observed, however, in series of shots (in which the density is not reproducible but increases from shot to shot) that the resonant surface moves further to the boundary when the density approaches the critical limit. It is therefore plausible that the critical parameter may not be the density limit but the location of the resonant surface within the confinement region.

For the above resonance the NBI heating is a definite precondition but the specific conditions (which may also be required) are not yet resolved. Sometimes the mode appears immediately when the NBI is switched on (Figure 7a), while in other cases the mode appears at a later time during the shot (Figure 7b). In every case, however, the boundary

iota has been in the range: $i(a) = 0.325 - 0.36$, which is close to the $i(a) = 0.33$ resonant value. Low frequency $m = 3$ modes (Figure 8), observed in the same iota range without any pronounced correlation to the NBI operation, rotate in the direction of the ExB drift (opposite to the high frequency mode rotation).

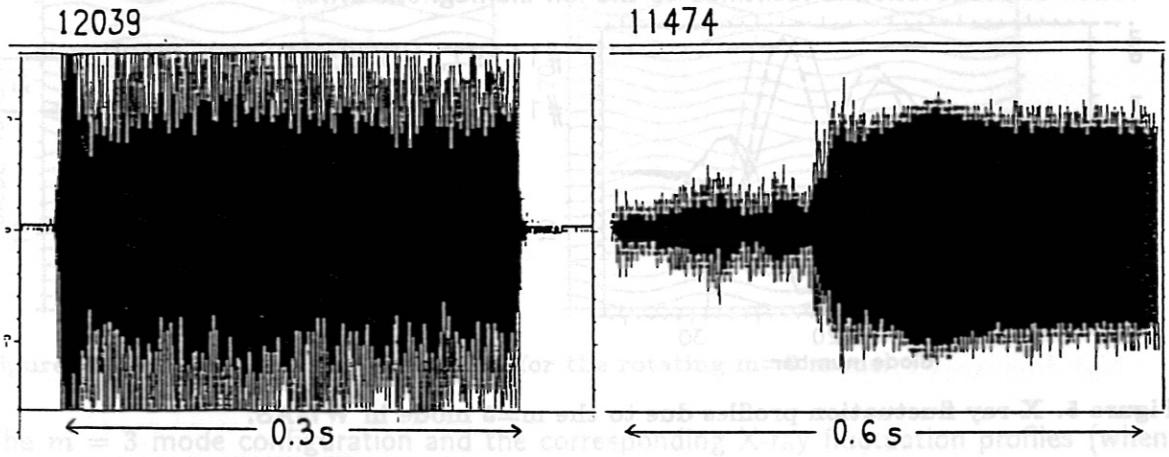

Figure 7(a/b). Magnetic fluctuations during the entire shot in W7-AS.

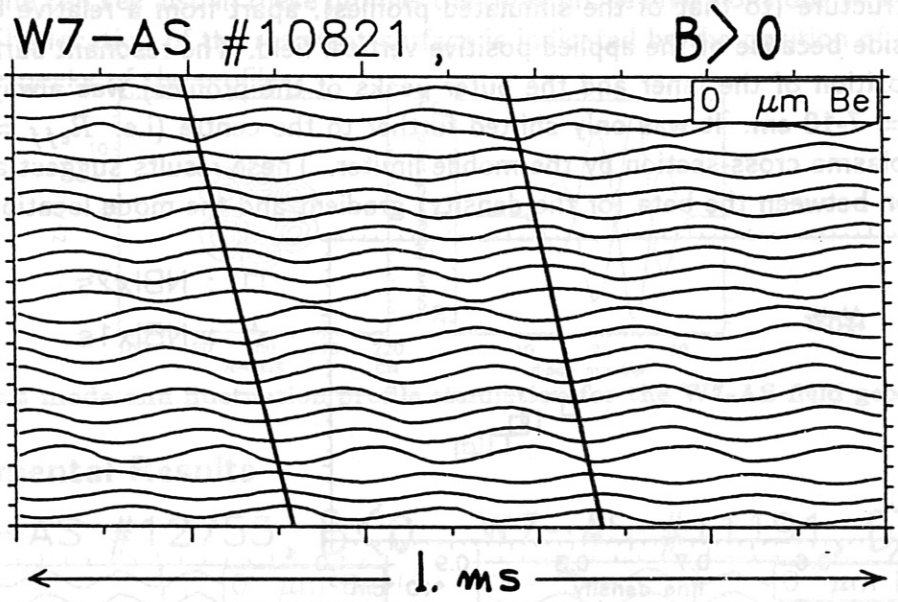

Figure 8. X-ray fluctuations due to the m=3 low frequency mode.

4. Conclusions

The reproducibility of the mode characteristics and its correlation with the NBI operation lead to the conclusion that this is an NBI-driven effect different from the $m = 2$, $m = 3$ modes earlier observed (the difference in the frequency spectrum is the gap of 5-20 kHz). Fast beam-ions are possibly involved but the physics for this resonance and its inpact on transport are presently under investigation.

References

[1] A. Weller et al: EPS Amsterdam (1990)

SIMULATION OF THE INFLUENCE OF COHERENT AND RANDOM DENSITY FLUCTUATIONS ON THE PROPAGATION OF ECRH-BEAMS IN THE W7AS STELLARATOR

M. Tutter, V. Erckmann, U. Gasparino, and the W7AS-Team
Max-Planck-Institut für Plasmaphysik, EURATOM-Association, 8046 Garching, Germany

In the W7AS stellarator the ECRH power is radiated to the plasma by 4 launchers (70 GHz, 200 kW each) arranged in pairs, which are separated azimuthually by about 5 degrees. The launchers of each pair are situated one upon another and normally radiate perpendicularly to the plasma, their beams crossing at the plasma axis.

In order to measure the spreading and the single pass absorption of the incoming beams, crossed arrays of microwave pick-up antennas are installed in the torus wall opposite to each launcher, where the beams hit in case of small diffraction.

For a theoretical understanding of the experiment a ray tracing computer program was used which can model the spreading by plasma diffraction and the absorption of the launched microwave-beams.

We restrict the analysis to an experimental situation with only one gyrotron operating, i.e. one launcher is active, the power propagating in the (fundamental) ordinary mode. Fig. 1 shows the measured signals of the central channels of the two arrays in one poloidal plane. The upper signal is measured by the array opposite to the working launcher, which is directly hit by the beam. The dotted line is the line density. With increasing density the lower signal increases from very low values. Whereas the decrease of the upper signal can be understood because a) the absorption grows and b) the microwave beam is bent away by diffraction, the lower signal cannot be modelled by ray tracing, as long as we assume smooth density profiles as obtained by fitting measured values (Thomson scattering). The ray is bent in such direction, that the lower signal in the figure should also decrease, it should then not have risen above zero.There are no indications for contribution from multiple reflections between the walls, which should be strongest at low density.

We can model the observed lower signal by a fluctuating component superposed to the smoothed density. These fluctuations are treated as frozen and the results are then obtained through an average of several runs with different fluctuation patterns /1/.

As a result of the calculations coherent poloidal waves tend to broaden the incoming beam similarly to random fluctuations of comparable wavelength and amplitude, whereas radial waves (wave vectors mainly parallel to the beam) are much less effective, as expected.

Fig. 2 shows the results of a simulation with random fluctuations. The solid line is the signal received by the pick-up antenna opposite to the beam in absence of density fluctuations. The crosses and circles refer to the case with fluctuations and represent the signal picked up opposite and displaced, respectively.

Note that the direct and the scattered signal get closer and closer with increasing central density, i.e. the power gets more and more equally distributed after the transit through the plasma.

From Fig. 1 we find a difference between strong and weak signal of about 12 dB when the line density is at maximum (1.5×10^{19} m^{-2}). This corresponds to a central density of roughly 2.5 $\times 10^{13}$ cm^{-3} (the cutoff-density being 6×10^{13} cm^{-3}), for which we find in Fig. 2 the same difference of about 12 dB between direct and refracted signal.

For this fit a fluctuation level of 15% of the local unperturbed density has to be assumed. The used maximum k-value of these fluctuations was $2\pi \times 0.333$ cm^{-1}, depending on the 1.5 cm step of the grid in the ray-tracing code.

The required amplitude depends on the k-spectrum of the fluctuations (higher k being more efficient). The maximum investigable k in this approach is determined by the limit of applicability of geometrical optics itself, requiring perturbations with length scales much larger than the wave length of the propagating wave (in our case 4 mm).

To investigate the dependence of the fluctuation amplitude needed for a certain fit on the maximum k-value of the disturbance we took poloidal coherent waves the k-values of which could be varied. The result is shown in Fig. 3.

If we assume the fluctuation amplitude proportional to the gradient of the unperturbed density (instead of density itself) about the double fluctuation level (but now present only in the outer region of the plasma column) has to be taken.

Conclusions:

In the experiment described above we assume that the fluctuations are much faster than the rf bandwidth and the sampling frequency of the receivers. So we can observe only the time average of the real physical process.

The influence of density fluctuations is maximum in the neighbourhood of the cutoff-density.

Even if we assume the fluctuation amplitude proportional to the local density, we have to claim rather high relative amplitudes of 10 to 30 %, depending on the (unknown) k-spectrum.

These results are similar to those obtained from ECE measurements. (Density fluctuations can significantly change the average local absorption coefficient, which determines the EC emission /2/.)

References:

/1/ Hansen et al, Nucl. Fus. 28 (1988), 769.

/2/ H.J. Hartfuß, M. Tutter et al, 17th EPS Conf.Amsterdam 1990, IV, 1576.

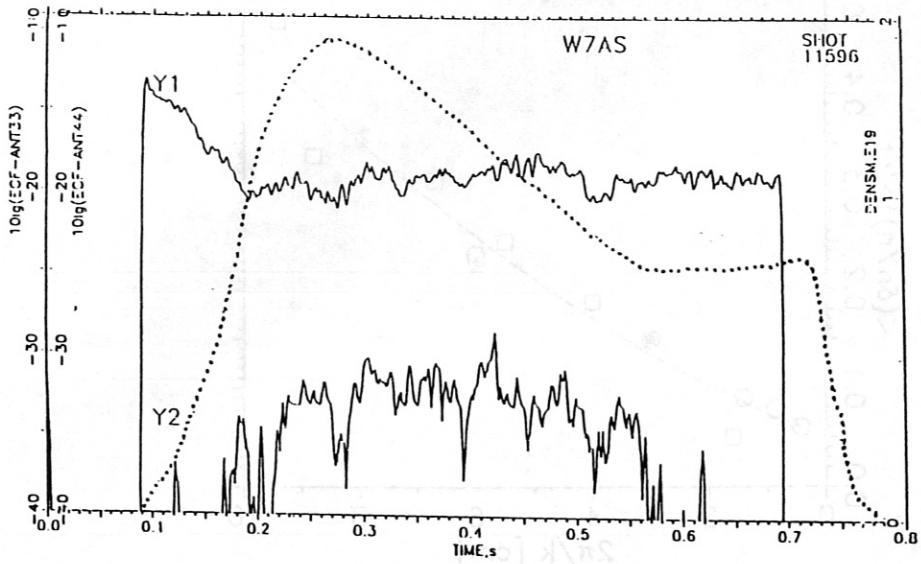

Fig. 1: Measured signals of pick-up antennas and line density (dotted) with one gyrotron working. The upper signal is that of the directly hit antenna.

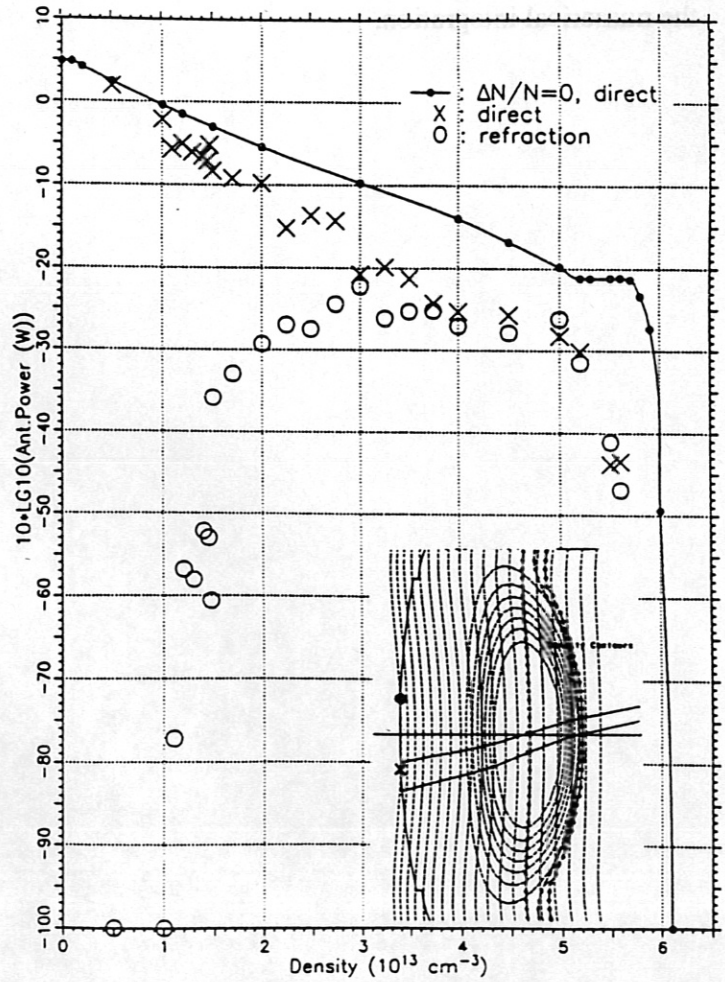

Fig. 2: Simulated signals.
The ECF-beam together with the positions of the two antennas is sketched in the insert.
Without fluctuations no signal is found in the upper antenna.

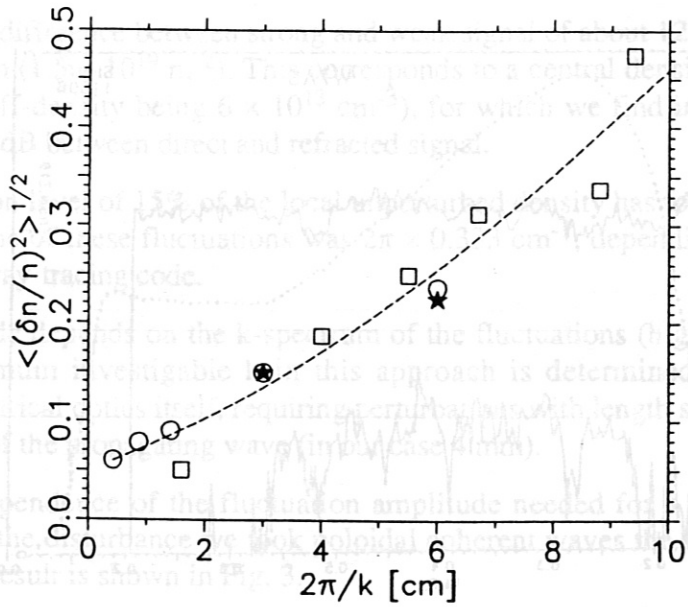

Fig. 3: Required amplitude vs. minimum wave length of the fluctuations to explain the results of Fig. 1. The stars refer to random fluctuations, the squares and the circles to poloidal coherent waves. The circles are evaluated in a 2-D slab limit to further increase the accuracy of the numerical integration.